Abouelezz, Amr; Stefen, Holly; Segerstråle, Mikael; Micinski, David; Minkeviciene, Rimante; Lahti, Lauri; Hardeman, Edna C.; Gunning, Peter W.; Hoogenraad, Casper C.; Taira, Tomi; Fath, Thomas; Hotulainen, Pirta

Tropomyosin Tpm3.1 Is Required to Maintain the Structure and Function of the Axon Initial Segment

Article

Tropomyosin Tpm3.1 Is Required to Maintain the Structure and Function of the Axon Initial Segment

Amr Abouelezz, Holly Stefen, Mikael Segerstråle, ..., Tomi Taira, Thomas Fath, Pirta Hotulainen

pirta.hotulainen@helsinki.fi

HIGHLIGHTS

Tropomyosin isoform Tpm3.1 co-localizes with the actin cytoskeleton in the AIS

Tpm3.1 inhibition led to a less organized AIS actin cytoskeleton

Perturbation of Tpm3.1 function reduced the accumulation of AIS scaffolding proteins

Tpm3.1 inhibition compromised cargo sorting and rapidly reduced firing frequency

CellPress
OPEN ACCESS

Article

Tropomyosin Tpm3.1 Is Required to Maintain the Structure and Function of the Axon Initial Segment

Amr Abouelezz,[1,2] Holly Stefen,[3] Mikael Segerstråle,[4] David Micinski,[1] Rimante Minkeviciene,[1] Lauri Lahti,[5] Edna C. Hardeman,[3] Peter W. Gunning,[3] Casper C. Hoogenraad,[6] Tomi Taira,[7] Thomas Fath,[3,8] and Pirta Hotulainen[1,9,*]

SUMMARY

The axon initial segment (AIS) is the site of action potential initiation and serves as a cargo transport filter and diffusion barrier that helps maintain neuronal polarity. The AIS actin cytoskeleton comprises actin patches and periodic sub-membranous actin rings. We demonstrate that tropomyosin isoform Tpm3.1 co-localizes with actin patches and that the inhibition of Tpm3.1 led to a reduction in the density of actin patches. Furthermore, Tpm3.1 showed a periodic distribution similar to sub-membranous actin rings but Tpm3.1 was only partially congruent with sub-membranous actin rings. Nevertheless, the inhibition of Tpm3.1 affected the uniformity of the periodicity of actin rings. Furthermore, Tpm3.1 inhibition led to reduced accumulation of AIS structural and functional proteins, disruption in sorting somatodendritic and axonal proteins, and a reduction in firing frequency. These results show that Tpm3.1 is necessary for the structural and functional maintenance of the AIS.

INTRODUCTION

The proximal ends of axons in the vertebrate nervous system contain the axon initial segment (AIS). The AIS serves as the site of action potential initiation and plays a role in maintaining neuronal polarity. The clustering of sodium channels at the AIS facilitates spike generation (Kole et al., 2008), whereas its role in maintaining polarity is the result of a vesicle filter and diffusion barrier that restrict the entry of dendritic proteins and membrane lipids into the axon (Brachet et al., 2010; Nakada et al., 2003; Song et al., 2009; Sun et al., 2014; Winckler et al., 1999). The AIS is a remarkably stable structure comprising a specialized membrane and protein complex. Central to this complex is ankyrin G (Kordeli et al., 1995; Rasband, 2010), which acts as an adaptor that recruits other AIS proteins (Jenkins and Bennett, 2001); ankyrin G recruits and binds to βIV-spectrin (Yang et al., 2007), neurofascin-186 (NF-186) (Ango et al., 2004), as well as sodium (Zhou et al., 1998) and KCNQ2/3 channels (Pan et al., 2006). The loss of ankyrin G leads to the loss of all other AIS components (Hedstrom et al., 2008; Jenkins and Bennett, 2001; Zhou et al., 1998). The interaction of ankyrin G with microtubules (Freal et al., 2016; Kuijpers et al., 2016; Leterrier et al., 2011) and the binding of βIV-spectrin to actin filaments (Jenkins and Bennett, 2001; Leterrier et al., 2015) link the AIS complex to the cytoskeleton.

Although recent studies have shed light on the role of microtubules in establishing and maintaining the AIS (Freal et al., 2016; Klinman et al., 2017; Kuijpers et al., 2016; van Beuningen et al., 2015), the precise role of actin in the AIS remains unclear (Papandreou and Leterrier, 2018). Proper AIS development requires an intact actin cytoskeleton (Xu and Shrager, 2005), but the mature AIS is insensitive to actin-disrupting drugs (Abouelezz et al., 2019; Jones et al., 2014; Leterrier et al., 2015; Qu et al., 2017; Sanchez-Ponce et al., 2011; Song et al., 2009). This suggests that actin has no role in maintaining the structure of the AIS. Alternatively, actin filaments in the AIS may be resistant to the action of actin-disrupting drugs owing to a low rate of turnover. Nonetheless, the integrity of the actin cytoskeleton is important for the AIS vesicle filter and diffusion barrier (Al-Bassam et al., 2012; Nakada et al., 2003; Song et al., 2009; Winckler et al., 1999). Platinum replica electron microscopy showed that the AIS contains both short, stable actin filaments and longer, dynamic filaments (Jones et al., 2014). Actin-based myosin motors play a role in the targeted delivery of

[1]Minerva Foundation Institute for Medical Research, Biomedicum Helsinki 2U, Tukholmankatu 8, 00290 Helsinki, Finland

[2]HiLIFE - Neuroscience Center, University of Helsinki, Haartmaninkatu 8, 00290 Helsinki, Finland

[3]School of Medical Sciences, UNSW Sydney, Sydney, NSW 2052, Australia

[4]Faculty of Biological and Environmental Sciences, University of Helsinki, Viikinkaari 1, 00790 Helsinki, Finland

[5]Department of Computer Science, Aalto University School of Science, Espoo, Finland

[6]Cell Biology, Department of Biology, Faculty of Science, Utrecht University, Padualaan 8, 3584CH Utrecht, the Netherlands

[7]Faculty of Veterinary Medicine, University of Helsinki, Agnes Sjöbergin katu 2, 00790 Helsinki, Finland

[8]Dementia Research Centre, Faculty of Medicine and Health Sciences, Macquarie University, Sydney, NSW 2109, Australia

[9]Lead Contact

*Correspondence: pirta.hotulainen@helsinki.fi

https://doi.org/10.1016/j.isci.2020.101053

somatodendritic and axonal vesicles (Janssen et al., 2017; Lewis et al., 2009, 2011), and actin filaments form patches in the AIS (Balasanyan et al., 2017; Watanabe et al., 2012) that may serve as cargo transport filters (Janssen et al., 2017; Leterrier and Dargent, 2014; Watanabe et al., 2012). Although actin patches are not exclusive to the AIS, AIS actin patches are more stable than patches along the distal axon; the washing away of diffuse molecules by cell permeabilization led to the loss of actin patches in the distal axon but not in the AIS (Watanabe et al., 2012). In addition, recent work showed that the actin-based non-muscle myosin II is involved in AIS structure and plasticity (Berger et al., 2018; Evans et al., 2017) and associates with axonal F-actin (Wang et al., 2020).

Super-resolution microscopy revealed the presence of periodic, sub-membranous, actin rings in the axon, forming a lattice with spectrin and ankyrin (D'Este et al., 2015; Leite et al., 2016; Leite and Sousa, 2016; Leterrier et al., 2015; Xu et al., 2013; Zhong et al., 2014). It was thought that axonal actin rings have similar molecular architecture than the erythrocyte membrane skeleton (Bennett and Baines, 2001; Leite et al., 2016; Leite and Sousa, 2016; Xu et al., 2013), where short, stable, adducin-capped actin filaments also form a sub-membranous lattice with spectrin and ankyrin (Fowler, 2013). Actin filaments in the erythrocyte membrane skeleton are also partly stabilized by tropomyosins (Fowler and Bennett, 1984; Sung et al., 2000; Sung and Lin, 1994). A recent study combining the super-resolution with platinum-replica electron microscopy, using mechanical unroofing of cells, brought new information of neuronal sub-membranous actin rings showing that actin rings are made of two long, intertwined actin filaments (Vassilopoulos et al., 2019).

Taken together, it is now well appreciated that the AIS contains two types of actin structures—patches and sub-membranous actin rings. Actin filaments forming actin rings are resistant to F-actin sequestering or severing drugs, suggesting they are stable (Abouelezz et al., 2019; Vassilopoulos et al., 2019). Currently, we lack information about the stability of F-actin in AIS actin patches. Furthermore, we know little about how the AIS actin cytoskeleton is regulated.

In this study, we show that the actin filaments in patches have a relatively slow turnover rate. The slow turnover rate of AIS actin filaments encouraged us to examine the potential role of tropomyosins. Tropomyosins are actin-binding proteins that form coiled-coil dimers and play a role in the regulation of the actin cytoskeleton in an isoform-specific manner (Gunning et al., 2008). Based on preliminary testing of available tropomyosin constructs, we focused studies on tropomyosin 3.1 (Tpm3.1). Tpm3.1 localizes to the axons of developing neurons and was suggested to play a role in neuronal polarity (Hannan et al., 1995; Vindin and Gunning, 2013; Weinberger et al., 1996). In addition, Tpm3.1 plays a role in regulating the filamentous actin pool in growth cones (Schevzov et al., 2008), growth cone motility (Fath et al., 2010), neurite branching (Schevzov et al., 2005), and neurite extension (Stefen et al., 2018). Tpm3.1 binds F-actin with high affinity (Gateva et al., 2017) and regulates the actions of key actin-binding proteins: (1) Tpm3.1 inhibits Arp2/3 complex-mediated polymerization (Kis-Bicskei et al., 2013); (2) Tpm3.1 enhances the phosphorylation of actin-depolymerizing factor/cofilin (Bryce et al., 2003) and inhibits the binding of cofilin to the pointed ends of actin filaments (Jansen and Goode, 2019), thus inhibiting filament severing as well as depolymerization at the pointed ends (Broschat, 1990; Jansen and Goode, 2019); (3) Tpm3.1 recruits tropomodulin to the pointed ends (Sung and Lin, 1994), further lowering the rate of depolymerization (Weber et al., 1994; Yamashiro et al., 2014); and (4) Tpm3.1 recruits and activates myosin II (Bryce et al., 2003; Gateva et al., 2017). Here, we show that tropomyosin 3.1 (Tpm3.1) is part of the AIS actin cytoskeleton and is necessary for the maintenance of AIS structure and function.

RESULTS

The AIS Contains Patches of F-Actin with a Low Rate of Depolymerization

Previous studies have revealed that actin forms patches in the AIS (Balasanyan et al., 2017; D'Este et al., 2015; Janssen et al., 2017; Jones et al., 2014; Leite et al., 2016; Leite and Sousa, 2016; Leterrier et al., 2015; Watanabe et al., 2012; Xu et al., 2013; Zhong et al., 2014) that may play a role in the filtering of somatodendritic cargo (Balasanyan et al., 2017; Janssen et al., 2017; Watanabe et al., 2012). However, little is known about the dynamics and regulation of these actin patches. To investigate F-actin dynamics in the AIS, we expressed photoactivatable GFP-tagged actin (PAGFP-actin) in cultured rat hippocampal neurons (Koskinen and Hotulainen, 2014; Patterson and Lippincott-Schwartz, 2002). We co-transfected neurons at 8–10 days *in vitro* (DIV) using mCherry and PAGFP-actin and imaged them 40–56 h later. To label the AIS, we used an antibody against the extracellular domain of NF-186, 1–2 h before imaging (Hedstrom et al., 2008). To visualize the distribution of F-actin in the AIS, we applied a brief 405-nm laser pulse within
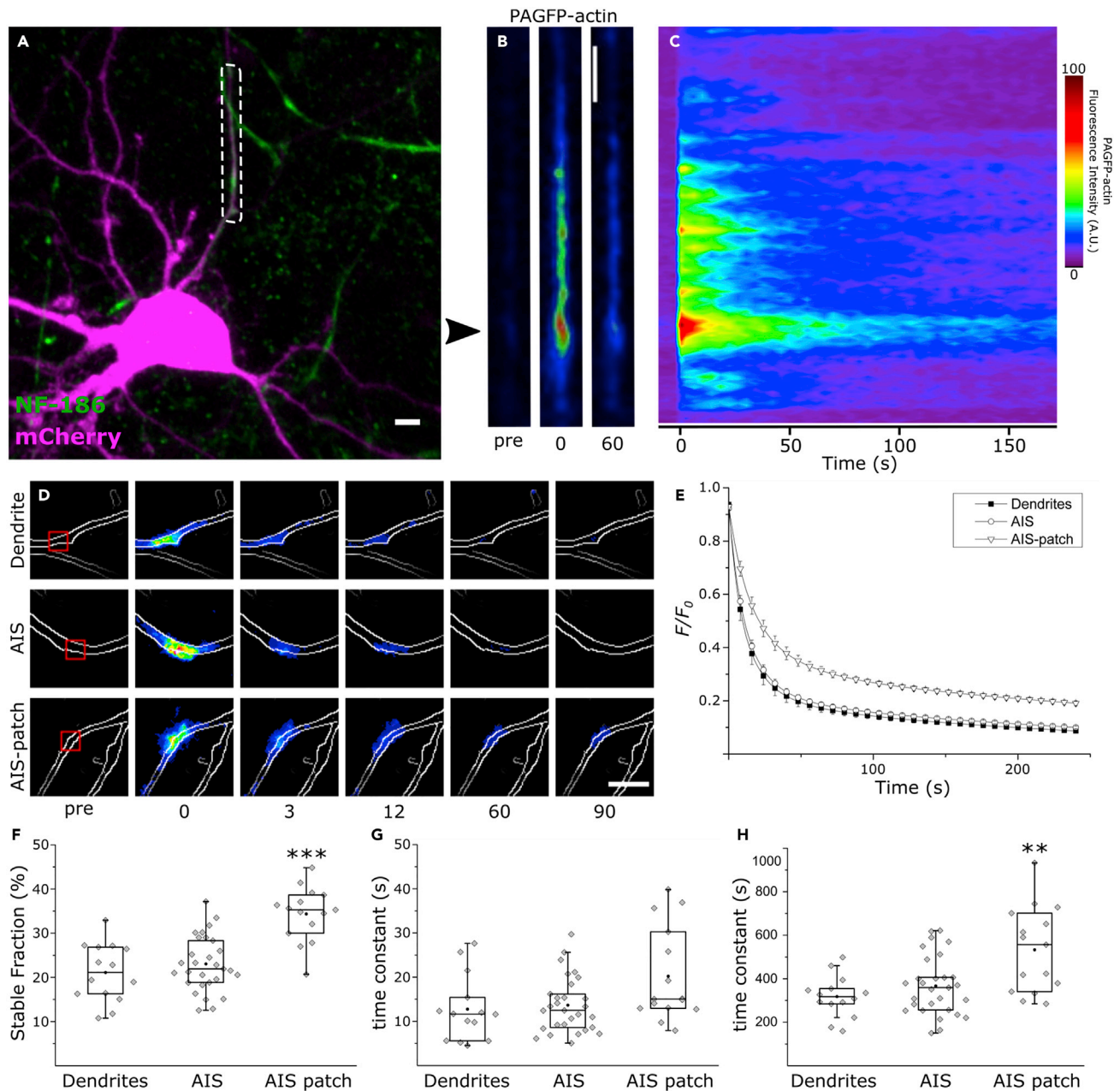
Figure 1. F-actin Patches in the AIS Have a Lower Rate of Depolymerization

(A) We performed photoactivation within the dashed box representing the entire AIS in rat hippocampal neurons expressing mCherry and PAGFP-actin and monitored PAGFP fluorescence over time. PanNF186 served to label the AIS.

(B) Higher magnification of the dashed box in (A) showing PAGFP-actin fluorescence 3 s before, immediately after, and 60 s after photoactivation. Arrowhead indicates F-actin patch.

(C) PAGFP-actin fluorescence intensity profile along the AIS over time.

(D) We performed photoactivation in a dendrite, the AIS, or an F-actin patch in the AIS ("AIS patch"). Photoactivation was limited to the small boxed region to enable a more accurate measurement of F-actin dynamics. Contour lines were constructed using mCherry fluorescence.

(E) Average normalized fluorescence decay curve fits over time in dendrites, the AIS, and F-actin patches in the AIS. We fit fluorescence decay curves to a double-exponential decay function and compared the fitting parameters across groups.

(F) Percentage of the stable fraction in dendrites, the AIS, and AIS actin patches (ANOVA, Tukey's test).

(G) Time constants of the dynamic fractions (Mann-Whitney U test).

(H) Time constants of the stable fractions (Mann-Whitney U test).

a 30-μm-long region along the AIS (Figure 1A). The fluorescence intensity within this region was monitored for 3 min by capturing a frame every 3 s. Owing to the fast rate of diffusion of free actin monomers, the first frame taken after photoactivation (0 s) enables the visualization of only those monomers that were immobilized by incorporation into an actin filament (Honkura et al., 2008).

The distribution of F-actin in the AIS was uneven and a prominent patch under 1 μm in diameter showed a higher fluorescence intensity, corresponding to a higher concentration of F-actin (Figure 1B). Relative to the rest of the AIS, this actin patch was also the most long-lived (Figure 1C). To measure the rate of depolymerization more accurately, we confined the photoactivation to a square area roughly 5 μm^2 in size (Figure 1D, red box). In addition to allowing for faster photoactivation, minimizing the area of photoactivation also minimizes the interference of photoactivated monomers that are incorporated into neighboring filaments after dissociation, leading to improved accuracy. Photoactivation was carried out within an AIS actin patch, in the AIS outside actin patches, and in a comparable dendritic segment that does not contain dendritic spines or branching points. An image was taken every 3 s and fluorescence intensity values were recorded. After subtracting the background fluorescence, we normalized the intensity values to the value at 0 s to obtain a normalized fluorescence decay curve. A double-exponential decay function gave the best fit for the decay curves in all groups (Koskinen and Hotulainen, 2014), indicating the presence of two pools of actin filaments with different rates of depolymerization. Accordingly, we fit the fluorescence decay curves to a double-exponential decay function (Figure 1E) and the fitting parameters were compared across groups.

The average proportion of the stable fraction of actin filaments (Figure 1F) was not significantly different between dendrites (21.1 $\pm$ 1.8%, mean $\pm$ SEM, n = 14, 4 independent experiments) and regions in the AIS outside the patches (23.0 $\pm$ 1.2%, mean $\pm$ SEM, n = 29, 6 independent experiments). Actin patches, however, had a higher proportion of stable filaments (34.4 $\pm$ 1.6%, mean $\pm$ SEM, n = 15, 7 independent experiments, p < 0.001, ANOVA, Tukey's test). In contrast, using the same experimental setup we found the proportion of stable actin filaments in dendritic spines to be 18% and 30% in cultured hippocampal neurons at 14 and 21 DIV, respectively (Koskinen et al., 2014). Figures 1G and 1H show the time constants for the dynamic and the stable pools of actin filaments, respectively. The average decay time constant of the dynamic pool was not significantly different between dendrites (12.76 $\pm$ 1.99 s, mean $\pm$ SEM, n = 14), regions in the AIS outside the patches (13.66 $\pm$ 1.16 s, mean $\pm$ SEM, n = 29), and actin patches (20.2 $\pm$ 2.74 s, mean $\pm$ SEM, n = 15, Mann-Whitney U test, Bonferroni corrected). The average decay time constant for the stable pool was not significantly different between dendrites (318 $\pm$ 25 s, mean $\pm$ SEM, n = 14) and regions in the AIS outside the patch (367 $\pm$ 25 s, mean $\pm$ SEM, n = 29). This value was higher in the actin patches (533 $\pm$ 50 s, mean $\pm$ SEM, n = 15, p < 0.01, Mann-Whitney U test, Bonferroni corrected) indicating that filaments in the AIS actin patches have a lower rate of depolymerization. It is likely that sub-membranous actin rings in the AIS had a minimal contribution to the readout in these experiments. This is partly due to the relatively low amount of F-actin in the sub-membranous lattice compared with intracellular F-actin within the area activated (10-fold less overall F-actin, Figure S1). In addition, actin filaments in the sub-membranous rings are relatively stable (Abouelezz et al., 2019; Vassilopoulos et al., 2019), possibly leading to a low rate of incorporation of PAGFP-actin monomers available for photoactivation. These data indicate that the AIS contains patches of F-actin that have a high proportion of stable filaments with a low rate of depolymerization.

Tropomyosin Isoform Tpm3.1 Co-localizes with Actin Patches with Slow Turnover Rate

The slow depolymerization rate suggests that AIS actin patches either contain relatively long actin filaments or are stabilized by actin-binding proteins. Tropomyosins are a family of actin-binding proteins that align along actin filaments and affect their characteristics. In neurons, altogether 12 isoforms are expressed (Gray et al., 2017; Abouelezz et al., 2019; Al-Bassam et al., 2012; Ango et al., 2004; Bach et al., 2009; Balasanyan et al., 2017) from *Tpm1*, *Tpm3*, and *Tpm4* genes. We examined the localization of available tropomyosin constructs, and from tested constructs, only Tpm3.1 was present in the AIS. YFP-Tpm3.1 expression showed
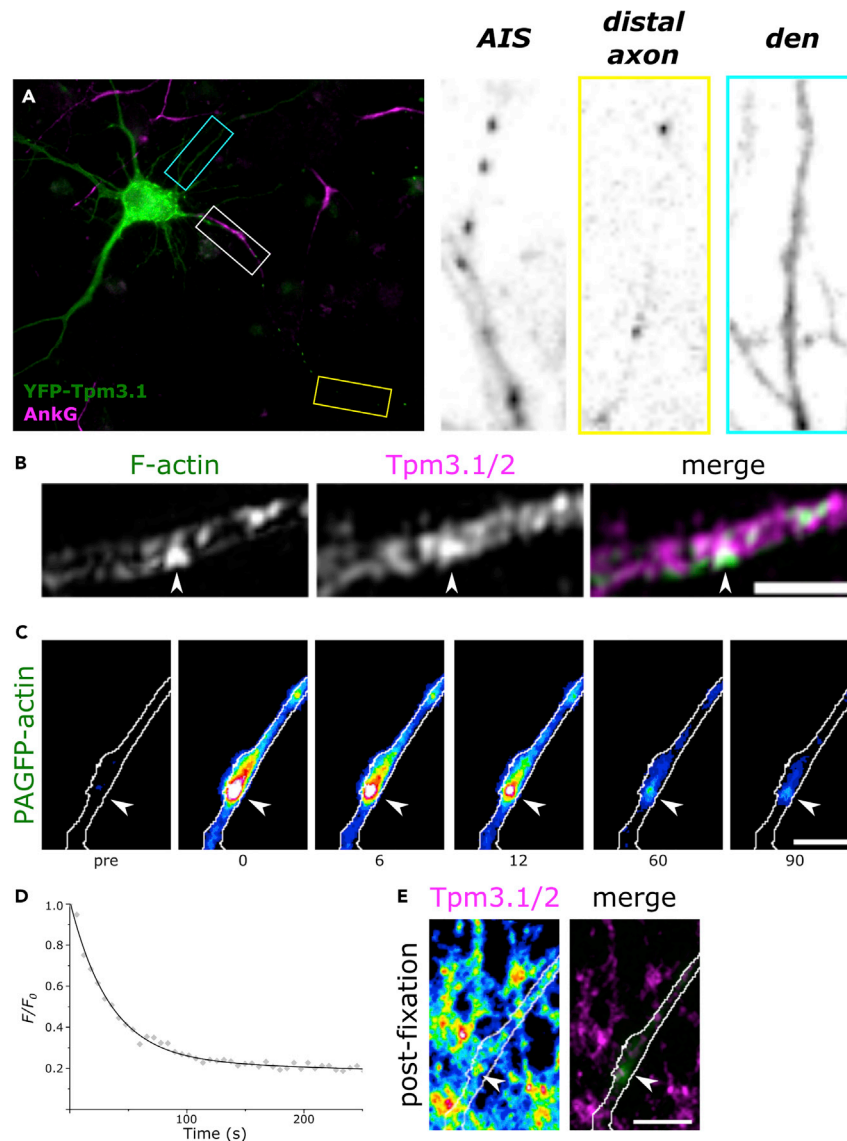
Figure 2. Tropomyosin Tpm3.1 Decorates Actin Patches in the AIS

(A) Rat hippocampal neuron expressing YFP-Tpm3.1. Neurons were fixed 8 h post transfection. Anti-ankyrin G served to label the AIS. Patches of YFP-Tpm3.1 can be seen in the AIS (white box) and distally in the axon (yellow box), whereas the somatodendritic domain (cyan box) shows a diffuse, less intense distribution.

(B) Maximum intensity projection of 3D-SIM reconstructions for F-actin and Tpm3.1/2. Arrowheads indicate actin patch. Scale bar: 1 μm.

(C) Actin patch visualized in live hippocampal neuron using PAGFP-actin before photoactivation (pre), immediately after activation (0 s), and the time-points indicated in seconds. Arrowheads indicate actin patch.

(D) Fluorescence decay over time (gray diamonds) of the actin patch in (C) and a double-exponential decay fit (solid black line).

(E) Tpm3.1/2 distribution visualized using anti-γ/9d in the same area after fixation in 4% PFA. The intensity of Tpm3.1/2 immunofluorescence was higher in the region corresponding to the actin patch visualized in (C) (arrowhead). Scale bar: 5 μm.

See also Figure S2.

bright puncta in the AIS and the distal axon and a diffuse distribution in the somatodendritic domain (Figure 2A). In contrast, the expression of the closely related YFP-tagged tropomyosin isoform Tpm3.2 (sharing 7 of 8 exons) showed a faint and diffuse distribution in the AIS and distal axon and mild enrichment in dendritic spines (Figure S2A). Therefore, we focused our further experiments on Tpm3.1.

We next wanted to test whether endogenous Tpm3.1 shows a similar staining pattern as YFP-Tpm3.1 and whether Tpm3.1 patches co-localize with actin patches. Epifluorescence imaging of anti-Tpm3.1/2 antibody γ/9d-staining showed patchy labeling (Figure S2B). Super-resolution structured illumination microscopy (SIM) imaging of phalloidin and γ/9d-antibody staining distribution revealed that patchy distribution of F-actin and Tpm3.1 co-localized (Figure 2B). γ/9d-antibody recognizes both Tpm3.1 and Tpm3.2, but as Tpm3.2 was absent from the AIS, we assumed that the fluorescence intensity detected using this antibody in the AIS originates from binding of Tpm3.1. Furthermore, we used PAGFP-actin to locate an actin patch with a low rate of depolymerization, then used anti-γ/9d to examine Tpm3.1 distribution. Tpm3.1 immunofluorescence showed a high intensity at the actin patch with slow PAGFP-actin fluorescence decay (Figure 2C, arrowheads), indicating that Tpm3.1 colocalizes with actin patches in the AIS (Figure 2E). Conversely, Tpm3.1 patches were resistant to detergent extraction (Figure S2C), indicating cytoskeletal association. On average, the intensity of Tpm3.1 was 2.5 times higher in patches than in the AIS overall, including patches (mean ± SEM: 2.52 ± 0.18, n = 25, 5 independent experiments). Based on these data, we conclude that Tpm3.1 is present in the AIS and co-localizes with actin patches.

Tropomyosin Isoform Tpm3.1/2 Is Part of the Periodic AIS Actin Cytoskeleton

In addition to patches, actin filaments in the AIS organize into periodic, sub-membranous rings, forming a lattice with spectrin and ankyrin (D'Este et al., 2015; Leite et al., 2016; Leite and Sousa, 2016; Leterrier et al., 2015; Xu et al., 2013; Zhong et al., 2014). We used SIM to test if Tpm3.1 also decorated actin filaments in these sub-membranous rings in cultured rat hippocampal neurons at 14 DIV. We used anti-γ/9d and Alexa 488-tagged phalloidin to visualize Tpm3.1 and F-actin, respectively. Anti-ankyrin G served to label the AIS. We optimized imaging parameters to visualize anti-γ/9d, tagged using Alexa 647. Similar to sub-membranous F-actin, Tpm3.1 showed a periodic distribution in the AIS (Figure 3A). To quantify the periodicity of Tpm3.1, we plotted fluorescence intensity profiles along regions in the AIS with visible periodicity and calculated the autocorrelation function for each profile. The average autocorrelation for the profiles measured showed an autocorrelation peak at a lag of 200 nm for both F-actin and Tpm3.1 (Figures 3B and 3C, left panels). Owing to the pixel size of the camera used (40 nm), the distances recorded are multiples of 40. Accordingly, a lag of 200 nm corresponds to the ~190 nm reported earlier for actin rings and other components of the AIS sub-membranous lattice (D'Este et al., 2015; Leite et al., 2016; Leterrier et al., 2015; Xu et al., 2013; Zhong et al., 2014). For both F-actin and Tpm3.1, we measured the distance between individual neighboring fluorescence intensity peaks in each profile (Figures 3B and 3C, right panels). The mean inter-peak distance for F-actin was 190.36 ± 1.7 nm (mean ± SEM), with 37.7% of the profiles 200 nm apart. The mean inter-peak distance for Tpm3.1 was 200.98 ± 1.5 nm (mean ± SEM), with 47.1% of the distances measuring 200 nm. In distal axons and dendrites, Tpm3.1 showed less uniform periodicity compared with the AIS (Figure S3). Despite the similar inter-peak distance between F-actin and Tpm3.1 in the AIS, their distribution was only partially overlapping (Figure S4). Taken together, Tpm3.1 shows similar periodicity with sub-membranous F-actin rings. Tpm3.1 periodicity is most uniform in the AIS, whereas dendrites and distal regions of axons show less strict periodicity. The partial overlap of actin and Tpm3.1 suggests that Tpm3.1 is linked to sub-membranous actin rings but actin ring filaments are not necessarily aligned with Tpm3.1.

Tpm3.1 Is Required for Maintaining the Structure of the AIS

We next examined the consequences of the perturbation of Tpm3.1 function for AIS structure. We used two distinct, well-characterized, small-molecule Tpm3.1 inhibitors, namely, TR100 (Bonello et al., 2016; Kee et al., 2015, 2018; Stehn et al., 2013) and Anisina (ATM3507) (Currier et al., 2017; Janco et al., 2019; Stehn et al., 2016) to inhibit Tpm3.1 and examined the accumulation of ankyrin G and other AIS markers at the AIS in mature cultured rat hippocampal neurons. TR100-mediated inhibition of Tpm3.1 does not inhibit the binding of Tpm3.1 to actin filaments but negates its effect on the rate of depolymerization (Bonello et al., 2016). The effects of TR100 on glucose-stimulated insulin secretion from the pancreatic islets were not seen in Tpm3.1 knockout mice, indicating that the impact of TR100 on glucose-stimulated insulin secretion was on-target (Kee et al., 2018). Similarly, Anisina (ATM3507) incorporates into the four-helix coiled coil overlap junction of the Tpm3.1 dimer as it binds to actin filaments, changing its lateral movement along the actin filament and altering the interactions of the actin filament with actin-binding proteins and myosin motors (Janco et al., 2019).

We incubated sparse cultures of rat hippocampal neurons at 10 DIV using DMSO (0.2%), TR100 (10 or 15 μM), or Anisina (5 or 7.5 μM) for 2, 3, or 6 h and then used anti-ankyrin G to visualize the distribution
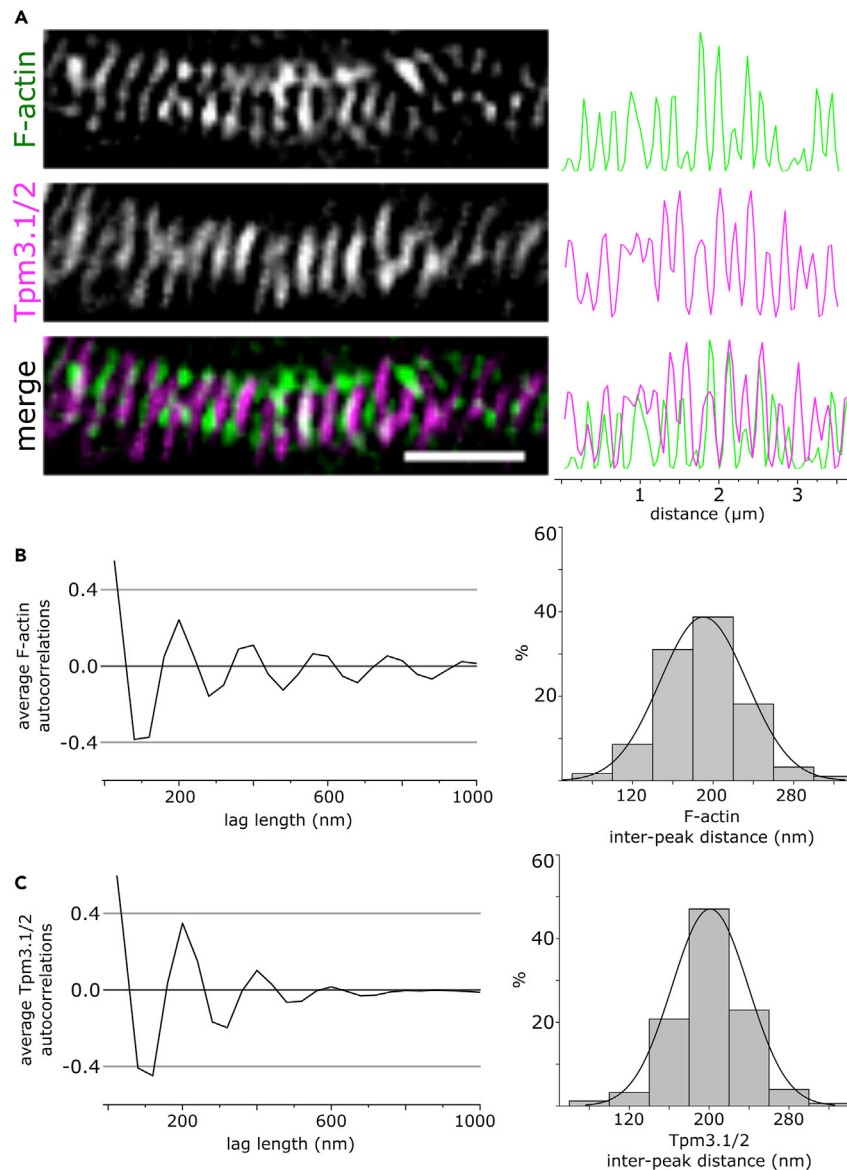
Figure 3. Tropomyosin Isoform Tpm3.1 Forms a Periodic Structure in the AIS

(A) SIM reconstruction of the AIS of a rat hippocampal neuron at 14 DIV labeled using anti-γ/9d and Alexa 488-tagged phalloidin to visualize Tpm3.1 and F-actin, respectively. Anti-Ankyrin G served to label the AIS. Tpm3.1/2 shows a periodic structure partially corresponding to actin rings in the AIS. Right: fluorescence intensity profile along the AIS.

(B) Left: Average autocorrelation of normalized phalloidin fluorescence intensity profiles showing autocorrelation at 200 nm. Right: Distance between individual peaks in normalized phalloidin fluorescence intensity profiles. About 37.7% of the peaks were separated by 200 nm.

(C) Left: Average autocorrelation of normalized anti-γ/9d fluorescence intensity profiles showing autocorrelation at 200 nm. Right: Distance between individual peaks in normalized anti-γ/9d fluorescence intensity profiles. About 47.1% of the peaks were separated by 200 nm. n = 25 cells, 4 independent experiments. Scale bar: 1 μm.

See also Figures S3 and S4.

of ankyrin G. Anti-MAP2 served to label the somatodendritic domain. Both TR100- and Anisina-mediated Tpm3.1 inhibition led to a notable reduction in the accumulation of ankyrin G at the AIS (Figure 4A). To quantify the reduction in ankyrin G accumulation, we blindly traced the fluorescence intensity profile of ankyrin G along the initial 30 μm of every neurite to calculate an AIS localization index (ALI, see Transparent Methods) (Figure 4B). For all treatment conditions, the ALI was lower than the corresponding DMSO
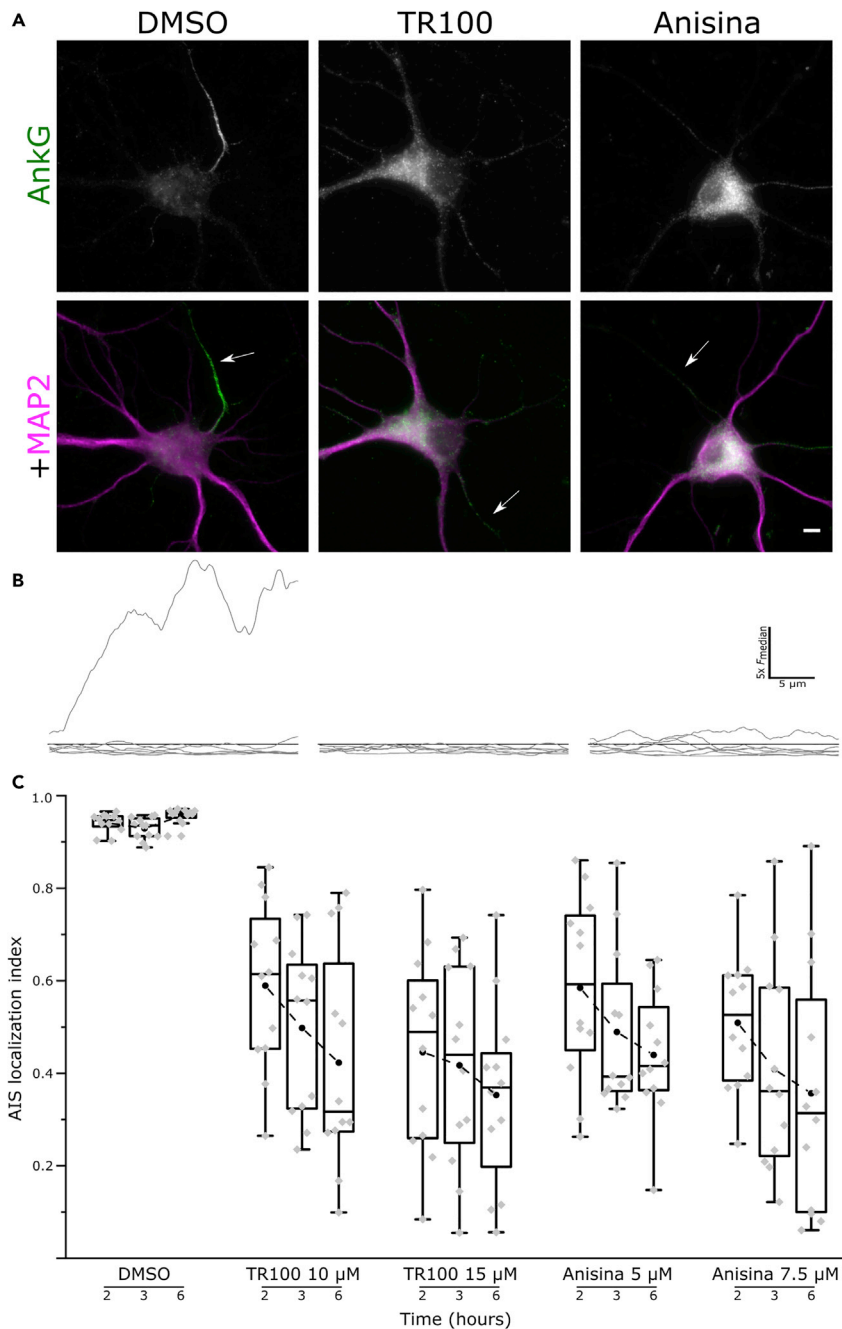
Figure 4. Inhibition of Tpm3.1 Reduces the Accumulation of Ankyrin G at the AIS

(A) Rat hippocampal neurons treated at 10 DIV using DMSO or the small-molecule Tpm3.1 inhibitors TR100 or Anisina (ATM3507) for 2, 3, or 6 h. Anti-MAP2 served to label the somatodendritic domain; anti-ankyrin G served to measure the accumulation of ankyrin G. Arrows point to axons.

(B) Smoothed ankyrin G fluorescence intensity line profiles (gray lines) along each neurite of the corresponding cell in (A), normalized to the median peak value (black line).

(C) AIS localization indices for neurons treated using DMSO, TR100 (10 or 15 μM), or Anisina (5 or 7.5 μM) for 2, 3, or 6 h. All treatment groups were significantly different from DMSO controls (Mann-Whitney U test; DMSO 0.2%, 2 h: 0.94 ± 0.006, mean ± SEM; DMSO 0.2%, 3 h: 0.93 ± 0.006; DMSO 0.2%, 6 h: 0.96 ± 0.005; TR100 10 μM, 2 h: 0.59 ± 0.050, $p < 0.001$; TR100 10 μM, 3 h: 0.50 ± 0.051, $p < 0.001$; TR100 10 μM, 6 h: 0.42 ± 0.066, $p < 0.001$; TR100 15 μM, 2 h: 0.45 ± 0.060, $p < 0.001$; TR100 15 μM, 3 h: 0.42 ± 0.060, $p < 0.001$; TR100 15 μM, 6 h: 0.35 ± 0.056, $p < 0.001$; Anisina 5 μM, 2 h: 0.58 ± 0.055, $p < 0.001$; Anisina 5 μM, 3 h: 0.49 ± 0.049, $p < 0.001$; Anisina 5 μM, 6 h: 0.44 ± 0.039, $p < 0.001$; Anisina 7.5 μM,

Figure 4. *Continued*

2 h: 0.51 ± 0.041, p < 0.001; Anisina 7.5 μM, 3 h: 0.41 ± 0.062, p < 0.001; Anisina 7.5 μM, 6 h: 0.36 ± 0.075, p < 0.001; for each treatment, n = 12, 3 independent experiments). The mean ALI of the treatment groups was negatively correlated with treatment duration and concentration. Black circles represent mean values. Box borders represent the 25th and 75th percentiles, whiskers represent minimum and maximum values less than 1.5x the interquartile range lower or higher than the 25th or 75th percentiles, respectively (Tukey style). Dotted lines connect mean values. Scale bar: 5 μm. See also Figure S5.

controls (Figure 4C). The mean ALI was negatively correlated with the concentration of both TR100 (Pearson's coefficient; 2 h: −1.0; 3 h: −0.98; 6 h: −0.97) and Anisina (Pearson's coefficient; 2 h: −0.99; 3 h: −0.98; 6 h: −0.98), as well as with the duration of the treatment (Pearson's coefficient; TR100 10 μM: −0.94; TR100 15 μM: −1.0; Anisina 5 μM: −0.90; Anisina 7.5 μM: −0.90), suggesting dose and time dependence. We similarly observed a reduction in the mean ALI of ankyrin G after overnight inhibition of Tpm3.1 (Figures S5A and S5B). Tpm3.1 inhibition also abolished the accumulation at the AIS of all other AIS markers tested, namely, TRIM46, EB1, and neurofascin-186 (Figures S5C–S5F).

Although the loss of AIS structure upon Tpm3.1 inhibition using either TR100 or Anisina was clear, it is possible that this was a secondary effect rising from a general decay in neuronal health rather than a direct effect of the perturbation of Tpm3.1 function. In fact, oxidative stress (Clark et al., 2017) and neuronal injury (Schafer et al., 2009) resulted in the disruption of the AIS in a calpain-mediated manner. Schafer et al. (2009) showed that neuronal injury induced irreversible AIS disassembly through calpain-mediated proteolysis of ankyrin G and βIV-spectrin. However, this process was blocked by using the calpain inhibitor MDL28170. Thus, to test whether a similar calpain-dependent mechanism contributes to the loss of the AIS upon Tpm3.1 inhibition, we added calpain inhibitors to TR100 or Anisina treatments and measured the ALI of ankyrin G. Indeed, the loss of AIS structure upon Tpm3.1 inhibition was calpain independent; the mean ALI for all treatment conditions did not significantly change in the presence of 100 μM of the calpain inhibitor MDL28170 for the entire duration of the treatment (Figure S5G).

To verify that the loss of ankyrin G accumulation at the AIS is a result of the loss of Tpm3.1 function, we generated a conditional knockout mouse model (Tp9 line, Figure S6, See Transparent Methods) for all Tpm3 isoforms containing exon 1b (namely, Tpm3.1, Tpm3.2, Tpm3.3, Tpm3.4, Tpm3.5, Tpm3.7, Tpm3.8, Tpm3.9, Tpm3.12, and Tpm3.13). We plated dissociated hippocampal neurons from these mice onto PDL-coated coverslips. To induce protein depletion, we transduced cultures using CMV-EGFP-Cre adeno-associated viruses (UNC Vector Core Facility). This resulted in a 10% transduction efficiency leading to a mixture of wild-type neurons and neurons with reduced Tpm3 level. Alternatively, we used CMV-EGFP adeno-associated viruses to transduce GFP—but not Cre—expression in sister cultures as controls. We confirmed the reduction of Tpm3 isoforms through immunostaining using an anti-Tpm3 antibody 2G10.2 (Figure S7). We then used anti-ankyrin G to visualize the accumulation of ankyrin G at the AIS. We first analyzed the intensity of ankyrin-G staining in GFP- or Cre-GFP-transfected cells (Figure 5B), and additionally, we analyzed the ALI as we did for TR100- and Anisina-treated cells (Figure 5C). The effect in cells from the conditional Tpm3 KO line with Cre expression was milder than that observed with the acute small-molecule inhibition. This milder effect is likely the result of residual Tpm3.1/2 present at the time of analysis.

As tropomyosins are a large family containing numerous isoforms obtained by alternative splicing from four different genes, we wanted to test whether the effect on ankyrin G accumulation at the AIS was tropomyosin gene specific or if knocking out any *Tpm* gene will lead to the same effect. Therefore, we repeated the experiment with conventional *Tpm4* knockout mice (Tp16 line) (Pleines et al., 2017). Neurons dissociated from this mouse line did not show any detectable difference in the accumulation of ankyrin G at the AIS (Figure S8). These data indicate that tropomyosin-dependent accumulation of ankyrin G at the AIS is *Tpm3* gene specific.

Furthermore, we obtained similar results by expressing short hairpin RNA (shRNA) specific to exon 9d for 4 days, which only depletes *Tpm3* isoforms Tpm3.1 and Tpm3.2 (Figures S9A–S9C). Similar to experiments carried out with conditional *Tpm3* knockout cells, Tpm3.1/2 protein level was only partially reduced, leading to an effect milder than that seen with acute inhibition of Tpm3.1. However, this effect was rescued by over-expressing YFP-tagged human Tpm3.1, which differs in sequence within the shRNA-targeting region, implicating that the shRNA-induced effect was indeed dependent on Tpm3.1 expression level (Figures S9D
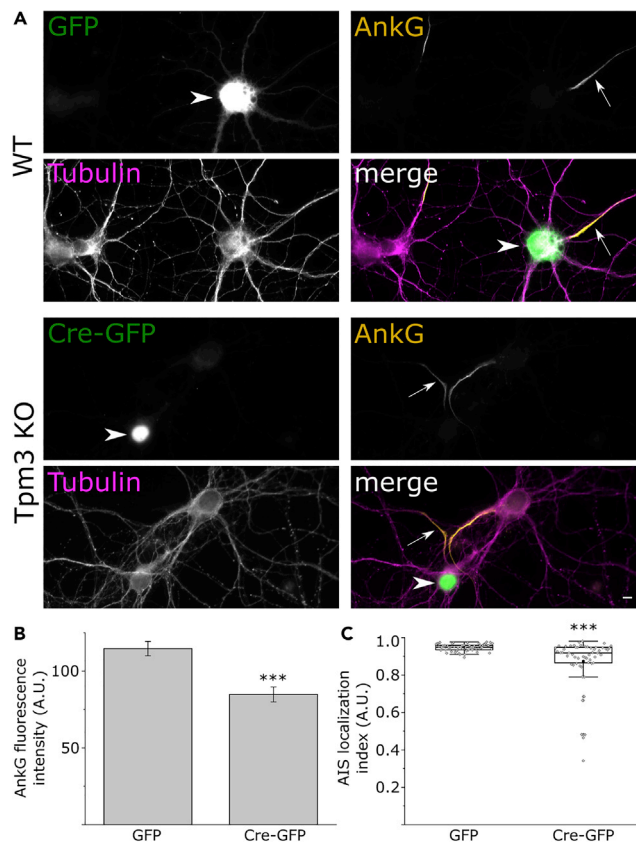
Figure 5. *Tpm3* **Conditional Knockout Neurons Show a Reduced Accumulation of Ankyrin G at the AIS**

(A) Ankyrin G immunofluorescence for GFP- (wild-type, WT) and Cre GFP-expressing (*Tpm3* KO) neurons. β3-Tubulin was used to label neurons. Arrowheads indicate transfected neurons; arrows indicate axons of transfected neuron. Scale bar: 5 μm.

(B) Average relative ankyrin G fluorescence intensity for each group (Mann-Whitney U test). Columns represent mean values. Error bars represent standard error of mean. GFP: n = 63, 3 independent experiments; Cre-GFP: n = 61, 3 independent experiments. * denotes statistical significance. ***: $p < 0.001$.

(C) AIS localization indices (ALI) for neurons infected with GFP or Cre-GFP. The ALI of Cre-GFP infected neurons (0.87 ± 0.02, mean ± SEM, n = 57, 3 independent experiments) was lower than that of GFP-infected controls (0.95 ± 0.002, mean ± SEM, n = 61, 3 independent experiment, $p < 0.001$, Mann-Whitney U test). Black circles represent mean values. Box borders represent the 25th and 75th percentiles, whiskers represent minimum and maximum values less than 1.5x the interquartile range lower or higher than the 25th or 75th percentiles, respectively (Tukey style).

See also Figures S6–S9.

and S9E). Thus, we conclude that both pharmacological inhibition and genetic depletion of Tpm3.1 cause a notable defect in AIS structure. Together, these data suggest that the reduced accumulation of ankyrin G at the AIS is the result of the loss of Tpm3.1 function, indicating that Tpm3.1 is necessary for maintaining the structure of the AIS.

Tpm3.1 Is Necessary for Maintaining the Selectivity of Axonal Transport and Sodium Channel Clustering at the AIS

Cargo transport filtering and the diffusion barrier at the AIS require an intact actin cytoskeleton (Song et al., 2009; Winckler et al., 1999). Somatodendritic cargo entering the AIS halt at regions of high F-actin concentration, in a process that is dependent on myosin motors (Balasanyan et al., 2017; Janssen et al., 2017; Watanabe et al., 2012). To test if Tpm3.1 is required for maintaining the AIS cargo transport filter, we fixed sparse cultures of rat hippocampal neurons at 10 DIV after an overnight treatment using DMSO (0.2%), LatB (5 μM), or TR100 (5 μM) and used antibodies against the somatodendritic glutamate receptor subunit GluA1 to visualize its distribution. Anti-MAP2 served to label the somatodendritic domain. Contrary to the somatodendritic localization of GluA1 observed in DMSO-treated neurons, we detected GluA1
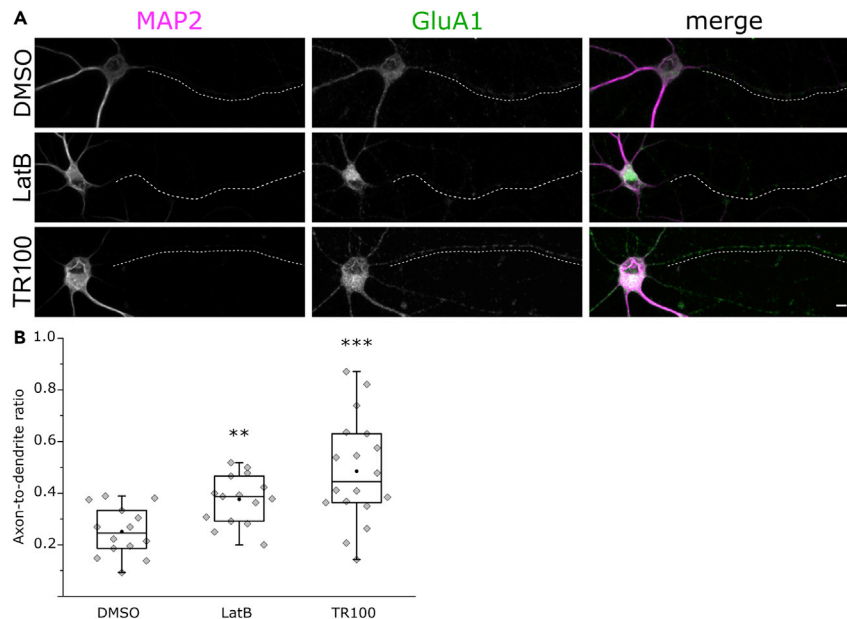
Figure 6. Tpm3.1 Inhibition Leads to the Redistribution of the Somatodendritic Marker GluA1

(A) MAP2 and GluA1 immunofluorescence in rat hippocampal neurons incubated overnight at 9–11 DIV in DMSO, LatB, or TR100. Dashed lines represent axons.

(B) GluA1 axon-to-dendrite ratios were higher in LatB- and TR100-treated neurons (Mann-Whitney U test). Black circles represent mean value. Box borders represent the 25th and 75th percentiles, whiskers represent minimum and maximum values less than 1.5x the interquartile range lower or higher than the 25th or 75th percentiles, respectively (Tukey style). DMSO 0.2%: n = 14, 2 independent experiments; LatB 5 μM: n = 15, 2 independent experiments; TR100 5 μM: n = 18, 2 independent experiments. * denotes statistical significance. **: $p < 0.01$; ***: $p < 0.001$. Scale bar: 5 μm.

immunofluorescence in both the dendrites and axons of treated neurons (Figure 6A). We used maximum intensity projection images from confocal stacks to blindly measure the mean fluorescence intensity along the axon and dendrites to calculate the axon-to-dendrite ratio for each group (Lewis et al., 2009). LatB-treated neurons showed a higher axon-to-dendrite ratio (0.38 ± 0.02, mean $\pm$ SEM, n = 15 neurons, 2 independent experiments, $p < 0.01$, Mann-Whitney U test) than DMSO-treated neurons (0.25 ± 0.03, mean $\pm$ SEM, n = 14 neurons, 2 independent experiments). TR100-treated neurons also showed a higher axon-to-dendrite ratio (0.49 ± 0.05, mean $\pm$ SEM, n = 18 neurons, 2 independent experiments, $p < 0.001$, Mann-Whitney U test) (Figure 6B). This suggests that Tpm3.1 function is necessary for maintaining the selectivity of axonal transport at the AIS.

In addition, we wanted to examine the effect of Tpm3.1 inhibition on the clustering of sodium channels, which is essential for spike generation at the AIS (Kole et al., 2008). This accumulation of channels is achieved through interactions with ankyrin G (Jenkins and Bennett, 2001; Zhou et al., 1998). We used antibodies against voltage-gated sodium channels (panNa$_v$) and the somatodendritic marker MAP2 to visualize sodium channel clustering at the AIS in sparse cultures of rat hippocampal neurons at 10 DIV after an overnight treatment using DMSO (0.2%), LatB (5 μM), or TR100 (5 μM). DMSO- and LatB-treated neurons showed clear detectable clustering of panNa$_v$ immunofluorescence in the AIS, whereas TR100-treated neurons displayed a relatively homogeneous distribution in all neurites (Figure 7A). To quantitatively examine this effect, we used maximum intensity projections of confocal stacks to blindly record panNa$_v$ immunofluorescence along the initial 30 μm of each neurite to calculate the ALI (Figure 7B). There was no difference in the mean ALI between DMSO-treated neurons (0.76 ± 0.02, mean $\pm$ SEM, n = 17 neurons, 3 independent experiments) and LatB-treated neurons (0.75 ± 0.03, mean $\pm$ SEM, n = 17 neurons, 3 independent experiments). In contrast, TR100-treated neurons showed a lower ALI (0.37 ± 0.04, mean $\pm$ SEM, n = 17 neurons, 3 independent experiments, $p < 0.001$, Mann-Whitney U test), indicating a more homogeneous distribution across neurites (Figure 7C). These data suggest that Tpm3.1 is required for the clustering of sodium channels at the AIS.
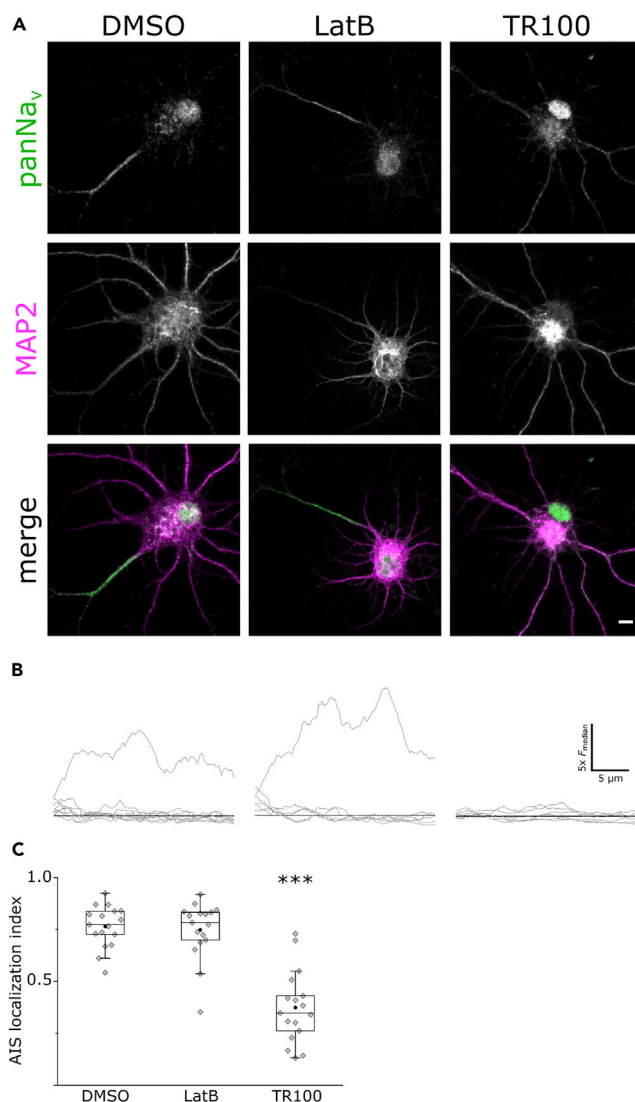
Figure 7. Tpm3.1 Inhibition Leads to the Loss of Voltage-Gated Sodium Channels Clustering at the AIS

(A) MAP2 and panNa$_v$ immunofluorescence in rat hippocampal neurons incubated overnight at 9–11 DIV in DMSO, LatB, or TR100.

(B) Smoothed panNa$_v$ fluorescence intensity line profiles (gray lines) along each neurite of the corresponding neuron in (A) normalized to the median value (black line).

(C) AIS localization indices for each group (Mann-Whitney U test). Black circles represent mean value. Box borders represent the 25th and 75th percentiles, whiskers represent minimum and maximum values less than 1.5x the interquartile range lower or higher than the 25th or 75th percentiles, respectively (Tukey style). DMSO 0.2%: n = 17, 3 independent experiments; LatB 5 μM: n = 17, 3 independent experiments; TR100 5 μM: n = 17, 3 independent experiments. * denotes statistical significance. ***: p < 0.001. Scale bar: 5 μm.

Tpm3.1 Inhibition Leads to a Reduction in Firing Frequency and Changes in Action Potential Properties

The initiation of action potentials is facilitated at the AIS by the clustering of ion channels (Kole et al., 2008) and is dependent on an intact AIS structure (Leterrier et al., 2017). To examine the effect of Tpm3.1 inhibition on spike generation, we recorded the activity of cultured rat hippocampal neurons at 16–18 DIV in current-clamp experiments in the presence of either DMSO (0.2%) or Anisina (2.5 μM). We introduced depolarizing steps of 100–200 pA at 10-s intervals and monitored the firing frequency 2 and 15 min after the introduction of DMSO or Anisina (Figure 8A). The mean firing frequency of DMSO-treated neurons remained unchanged 15 min after the introduction of DMSO (at 2 min: 18.3Hz ± 2.9, mean ± SEM; at
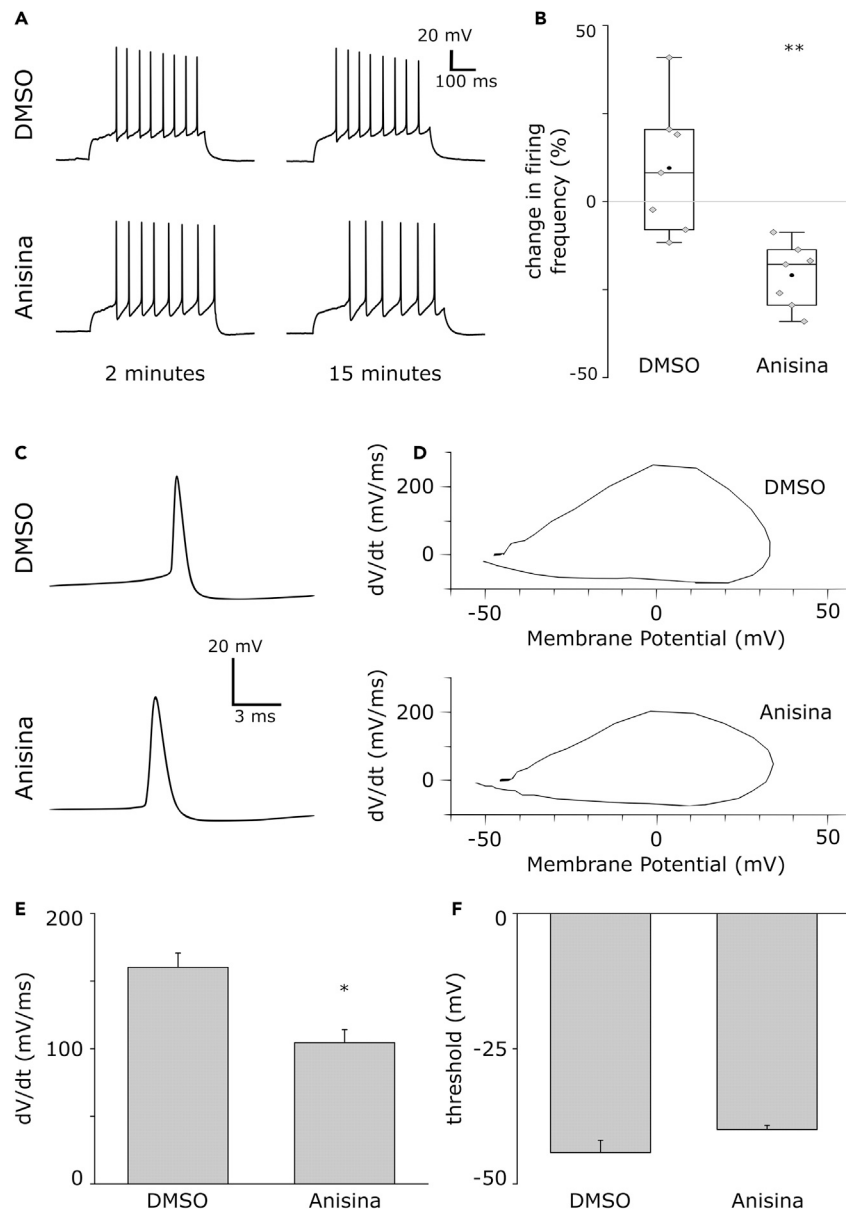
Figure 8. Tpm3.1 Inhibition Leads to a Reduction in Firing Frequency

(A) Individual traces from current-clamp (depolarizing step of 100 pA for 500 ms) recordings of rat hippocampal neurons in culture 2 and 15 min after treatments using either DMSO (0.2%) or Anisina (2.5 μM).

(B) The percentage change in firing frequency 15 min after introducing each treatment relative to the firing frequency at 2 min. Anisina-mediated inhibition of Tpm3.1 led to the attenuation of firing frequency 15 min after introduction. Black circles represent mean value. Box borders represent the 25th and 75th percentiles, whiskers represent minimum and maximum values less than 1.5x the interquartile range lower or higher than the 25th or 75th percentiles, respectively (Tukey style). DMSO 0.2%: n = 7, 5 independent experiments; Anisina 2.5 μM: n = 7, 5 independent experiments. * denotes statistical significance, two-sample t test. **: p < 0.01.

(C) Representative somatic membrane potential record of an action potential in a cultured hippocampal neuron. The action potential was elicited by current injection of 100 pA. Below, representative somatic membrane potential recording from a cultured hippocampal neuron with the Tpm3.1 inhibitor Anisina (2.5 μM) in the pipette filling solution.

(D) Phase plots, the first derivative of the somatic membrane voltage (dV/dt) versus membrane voltage (Vm) for control (DMSO, 0.2%) and Anisina-treated cultured hippocampal neurons.

Figure 8. *Continued*

(E) Summary of phase plot slopes 20 mV above threshold. Anisina-treated neurons show a shallower phase plot slope 104.50 ± 9.66 dV/dt compared with control neurons 160.15 ± 10.60, n = 5. * denotes statistical significance, two-sample t test. *: p < 0.05.

(F) Summary of action potential thresholds at 10 mV/ms; −44.19 ± 2.256 mV for control and −39.93 ± 0.77, p = 0.065 (two-sample t test), n = 5 for Anisina-treated cells, respectively.

15 min: 20.9Hz ± 4.2, mean ± SEM, n = 7 neurons, 5 independent experiments, paired-sample t test). Conversely, Anisina-treated neurons showed a significant attenuation of firing frequency after 15 min (at 2 min: 21.7Hz ± 4.2, mean ± SEM; at 15 min: 16.7Hz ± 2.6, mean ± SEM, n = 7 neurons, 5 independent experiments, p < 0.05, paired-sample t test). The change in mean firing frequency 15 min after introducing DMSO (9.5% ± 7.0, mean ± SEM) was significantly different from that of neurons treated using Anisina (−20.9% ± 3.4, mean ± SEM, p < 0.01, two-sample t test, Figure 8B).

To study the effects of Tpm3.1 inhibition by Anisina on action potential properties, we constructed phase plane plots using Clampex software (Figure 8D). Tpm3.1 inhibition resulted in a shallower phase plot slope 104.50 ± 9.66 dV/dt compared with control neurons 160.15 ± 10.60, p < 0.05, n = 5 (Figure 8E). The action potential threshold was slightly but not significantly lower in Anisina-treated neurons (−44.19 ± 2.256 and −39.93 ± 0.77 mV for control and Anisina-treated neurons, respectively, p = 0.065, n = 5) (Figure 8F). These data indicate that Tpm3.1 is required for maintaining AIS function in the initiation of action potentials, consistent with the loss of sodium channel clustering at the AIS.

Tpm3.1 Inhibition Leads to the Gradual Reduction in the Number of Actin Patches and Uniformity of Periodicity of the Sub-membranous Actin Rings

Our results show that Tpm3.1 is important for the accumulation of ankyrin G at the AIS, but it is not clear how Tpm3.1 inhibition leads to the loss of ankyrin G accumulation. We are not aware of any reports suggesting direct interaction between Tpm3.1 and ankyrin G. Thus, we hypothesized that the loss of Tpm3.1 function adversely affects the overall structure and organization of the actin cytoskeleton in the AIS. This disorganization would then ultimately lead to the loss of accumulation of ankyrin G and other structural AIS proteins (Hedstrom et al., 2008; Jenkins and Bennett, 2001; Zhou et al., 1998).

First, we tested the effect of Tpm3.1 inhibition on actin patches in the AIS. Tpm3.1 inhibition led to a reduction in the frequency of actin patches in the AIS compared with DMSO-treated neurons (DMSO: 0.58 ± 0.06 patches/μm, mean ± SEM, n = 13 neurons, 3 independent experiments; LatB: 0.71 ± 0.04 patches/μm, mean ± SEM, n = 13 neurons, 3 independent experiments, p = 0.19; TR100: 0.42 ± 0.02 patches/μm, mean ± SEM, n = 13 neurons, 3 independent experiments, p < 0.05; Anisina: 0.3 ± 0.05 patches/μm, mean ± SEM, n = 12 neurons, 3 independent experiments, p < 0.001, ANOVA, Tukey's test).

Next, we tested whether Tpm3.1 inhibition affects actin rings. We employed super-resolution microscopy techniques to examine the periodicity of F-actin in the AIS. We treated sparse cultures of rat hippocampal neurons at 14 DIV using DMSO (0.2%), TR100 (10 μM), or Anisina (5 μM) for 6 h. In addition, we treated cultures at DIV 13 using LatB (5 μM) overnight, similar to Winckler et al. (1999). Consistent with our earlier report (Abouelezz et al., 2019), LatB-treated neurons showed an overall lower phalloidin fluorescence intensity, reflecting a decrease in overall F-actin. Periodic actin rings were visible for all groups, indicating the persistence of the sub-membranous lattice, even in the absence of ankyrin G (Figure 9A). We blindly plotted fluorescence intensity profiles in regions within the AIS where periodicity was visible and calculated the autocorrelation function. All groups showed autocorrelation at a lag of 200 nm (Figure 9B). Owing to the pixel size of the camera used (40 nm), the distances recorded are multiples of 40. Accordingly, a lag of 200 nm corresponds to the ~190 nm reported earlier for actin rings and other components of the AIS sub-membranous lattice (D'Este et al., 2015; Leite et al., 2016; Leterrier et al., 2015; Xu et al., 2013; Zhong et al., 2014). In addition, we blindly measured the distance between individual peaks in each fluorescence intensity profile and compared the distribution of the inter-peak distances across groups (Figure 9C). About 54% of the inter-peak distances in DMSO-treated neurons were 200 nm, whereas the mean inter-peak distance was 192.49 ± 1.37 nm, mean ± SEM. The distribution of the inter-peak distances in LatB-treated neurons was not significantly different from DMSO controls, with 51.2% of the inter-peak distances at 200 nm and a mean inter-peak distance of 188.7 ± 1.38 nm, mean ± SEM (p = 0.47, Kolmogorov Smirnov
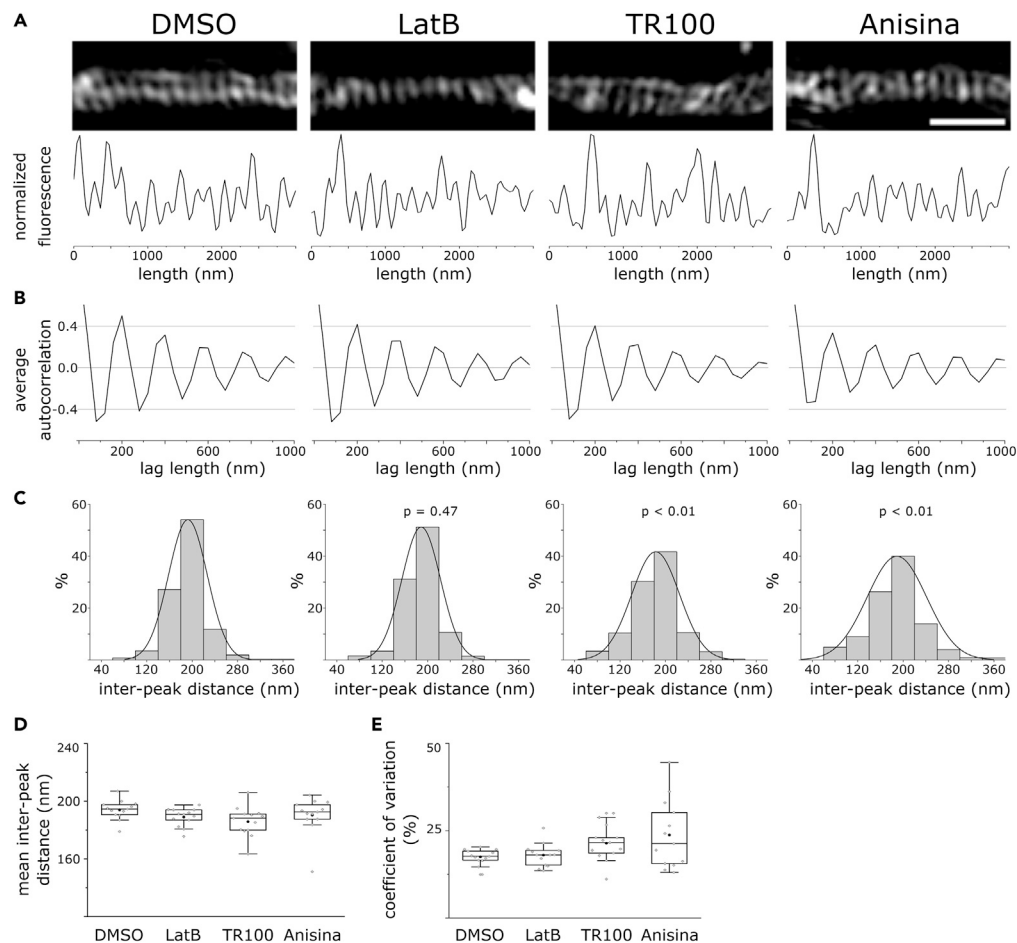
Figure 9. Tpm3.1 Inhibition Disrupts the Periodicity of Actin Rings in the AIS

(A) SIM reconstructions of F-actin in the AIS of neurons treated at 14 DIV using DMSO, LatB, TR100, or Anisina (ATM3507), visualized using Alexa 488-tagged phalloidin.

(B) Average autocorrelation of normalized fluorescence intensity profiles showing autocorrelation at 200 nm for all groups.

(C) Distribution of distances between individual peaks in fluorescence intensity profiles for each group. The distribution of inter-peak distances in TR100- and Anisina-treated neurons was significantly different (p < 0.01) from DMSO- and LatB-treated neurons (Kolmogorov-Smirnov test).

(D) The mean inter-peak distance and **e** coefficient of variation for individual cells in each group were not significantly different (Kruskal-Wallis ANOVA, p = 0.05 and p = 0.09, respectively). Black circles (D and E) represent mean value. Box borders represent the 25th and 75th percentiles, whiskers represent minimum and maximum values less than 1.5x the interquartile range lower or higher than the 25th or 75th percentiles, respectively (Tukey style). DMSO: n = 13 neurons, 4 independent experiments; LatB: n = 13 neurons, 4 independent experiments; TR100: n = 13 neurons, 3 independent experiments; Anisina: n = 13 neurons, 3 independent experiments. p values in (C) are relative to DMSO (Kolmogorov Smirnov test). Scale bar: 1 μm.

See also Figure S10.

test). In contrast, TR100-treated neurons showed a less uniform distribution with only 41.7% of the inter-peak distance at 200 nm and a mean inter-peak distance of 182.7 ± 1.74 nm, mean $\pm$ SEM (p < 0.01, Kolmogorov Smirnov test). Similarly, only 39.8% of the distances measured in Anisina-treated neurons were 200 nm, with a mean inter-peak distance of 189.0 ± 1.94 nm, mean $\pm$ SEM, a distribution significantly different from that of DMSO controls (p < 0.01, Kolmogorov Smirnov test). We also obtained similar results using stochastic optical reconstruction microscopy (STORM) (Figure S10). When calculated on a cell-by-cell basis, the mean inter-peak distance in each group was not significantly different (Kruskal-Wallis ANOVA, p = 0.05). The mean coefficient of variation was also not significantly different among groups (Kruskal-Wallis ANOVA, p = 0.09).
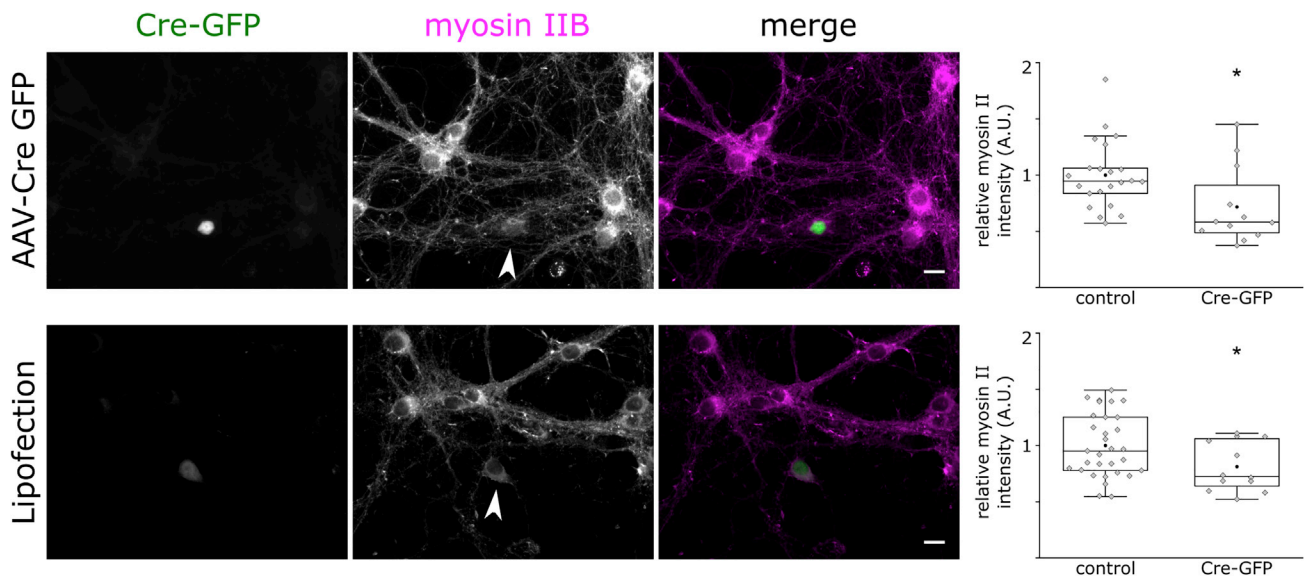
Figure 10. Loss of Tpm3.1 Leads to a Reduction in Myosin IIB Immunofluorescence

Cultured hippocampal neurons of conditional *Tpm3* knockout mice (Tp9 line). Arrowheads indicate neurons expressing Cre-GFP after either viral transduction (top panel) or lipofection (bottom panel). We used anti-myosin IIB to compare the distribution of myosin IIB in neurons expressing Cre-GFP and neighboring control neurons. Cre-GFP expressing neurons showed a lower intensity of myosin IIB immunofluorescence (t test). Box borders represent the 25th and 75th percentiles, whiskers represent minimum and maximum values less than 1.5x the interquartile range lower or higher than the 25th or 75th percentiles, respectively (Tukey style). Neurons expressing Cre-GFP; transduced: n = 12, 3 independent experiment; transfected n = 12, 3 independent experiments. Control neurons: transduced: n = 22; transfected: n = 31. * denotes statistical significance, two-sample t test. *: p < 0.05. Scale bar: 10 μm.

These results show that Tpm3.1 inhibition affects both AIS actin patches and actin rings. Tpm3.1 inhibition reduced the number of actin patches in the AIS, whereas LatB treatment increased their number. As shown before (Abouelezz et al., 2019), we found that the periodicity of sub-membranous actin rings in the AIS was resistant to LatB. As LatB disrupts the actin cytoskeleton through sequestering free actin monomers (thus inhibiting actin polymerization), stable actin filaments with a low rate of depolymerization may be less susceptible to LatB. In contrast, the inhibition of Tpm3.1 for the duration of the experiments (6 h) disrupted—but did not entirely abolish—the periodicity of sub-membranous actin rings. In addition to changing the uniformity of the periodicity, visual inspection revealed that actin rings were often tilted after Tpm3.1 inhibition, losing their nature of parallel transverse stripes (Figure 9A).

Tpm3.1 Depletion Reduces Myosin IIB Expression

The earlier experiments have mainly followed the idea that Tpm3.1 affects actin filament stability. However, in addition to playing a role in F-actin turnover, Tpm3.1 recruits and activates myosin IIB (Bryce et al., 2003; Gateva et al., 2017), and recent work has revealed an important role for myosin II in AIS structure (Berger et al., 2018; Evans et al., 2017; Wang et al., 2020). In U2 Osteosarcoma cells, Tpm3.1/3.2 overlaps with non-muscle myosin II heads but not with non-muscle myosin II tails or α-actinin in stress fibers (Meiring et al., 2019). Thus, we examined the effect of perturbing Tpm3.1 in cultured neurons on myosin IIB. We expressed Cre-GFP in cultured hippocampal neurons of *Tpm3* conditional knockout mice (Tp9 line) using either viral transduction or lipofection and used anti-myosin IIB to examine myosin IIB distribution (Figure 10). Neurons expressing Cre-GFP after viral transduction showed a lower intensity of myosin IIB immunofluorescence (0.72 ± 0.1, mean ± SEM, n = 12) relative to neighboring control neurons (1 ± 0.06, mean ± SEM, p < 0.05, two-sample t test, n = 22, 3 independent experiments). Similarly, compared with neighboring control neurons (1 ± 0.05, mean ± SEM, n = 31), neurons expressing Cre-GFP after lipofection showed a lower intensity of myosin IIB immunofluorescence (0.81 ± 0.06, mean ± SEM, p < 0.05, two-sample t test, n = 12, 3 independent experiments). The results are summarized in Figure 10.

DISCUSSION

Although an intact actin cytoskeleton is required for the formation of the AIS (Xu and Shrager, 2005), the mature AIS is remarkably stable and insensitive to actin-disrupting drugs (Jones et al., 2014; Leterrier

et al., 2015; Sanchez-Ponce et al., 2011; Song et al., 2009). This may lead to the conclusion that the actin cytoskeleton has no significant role in the maintenance of AIS structure. The loss of accumulation of ankyrin G (Figures 4, 5, S5, and S9) and other AIS structural (Figure S5) and functional proteins (Figure 7), disruption in sorting somatodendritic and axonal proteins (Figure 6), and a reduction in firing frequency (Figure 8) upon the perturbation of Tpm3.1 function, however, suggest otherwise.

The AIS actin cytoskeleton comprises sub-membranous actin rings and actin-rich patches (Papandreou and Leterrier, 2018). Although sub-membranous actin rings are not exclusive to the AIS (Bertling and Hotulainen, 2017; D'Este et al., 2015; Han et al., 2017; Leite et al., 2016; Leite and Sousa, 2016; Xu et al., 2013; Zhong et al., 2014), actin patches in the AIS are more numerous and resistant to extraction, compared with more distal axonal patches (Balasanyan et al., 2017). Our data suggest that Tpm3.1 co-localizes with actin patches in the AIS (Figure 2 and S2) and that the inhibition of Tpm3.1 led to a reduction in the number of AIS actin patches. In addition to patches, Tpm3.1 showed a periodic distribution similar to sub-membranous actin rings but Tpm3.1 was only partially congruent with sub-membranous actin rings (Figures 3 and S4). Nevertheless, the inhibition of Tpm3.1 affected the alignment of actin rings and the uniformity of their periodicity (Figures 9 and S10). In addition to rings and patches, axons have other less characterized actin structures such as actin trails or hotspots (Ganguly et al., 2015). As the distribution of Tpm3.1 was not congruent with sub-membranous actin rings (Figure S4), we propose that Tpm3.1 decorated actin filaments are partially actin filaments of actin rings but partially actin filaments outside the rings. Currently it is unclear what exactly are the Tpm3.1 decorated filaments outside the rings and patches. It is also possible that the inhibition of Tpm3.1 affects the recruitment and accumulation of other actin-binding proteins that are important for maintaining actin rings or other actin structures in the AIS. Although the exact mechanism is still unclear, our data show that Tpm3.1 provides support for the AIS structural complex.

Tpm3.1 Stabilizes Actin Filaments and Recruits and Activates Myosin II

Biochemically, Tpm3.1 was shown to have two main functions in actin filament regulation—it stabilizes actin filaments and regulates myosin IIB binding and contractility. Tpm3.1 enhances the phosphorylation (and inactivation) of actin-depolymerizing factor/cofilin (Bryce et al., 2003) and inhibits the binding of cofilin to the pointed ends of F-actin (Jansen and Goode, 2019), thus inhibiting filament severing as well as depolymerization at the pointed ends (Broschat, 1990). Furthermore, Tpm3.1 recruits tropomodulin to the pointed ends (Sung and Lin, 1994), further lowering the rate of depolymerization (Weber et al., 1994; Yamashiro et al., 2014). Thus, the inhibition of Tpm3.1 renders Tpm3.1-decorated actin filaments vulnerable to depolymerization (Bonello et al., 2016), and therefore, it is plausible that the loss of AIS structure upon Tpm3.1 inhibition is due to a reduction in the stability of actin filaments. Bach et al. (2009) showed that Tpm3.1 is required for stabilizing actin filaments in the formation and maturation of focal adhesions. Tpm3.1-decorated actin filaments are the least sensitive to latrunculin and Cytochalasin D (Creed et al., 2008; Percival et al., 2000). It is, therefore, expected that inhibiting Tpm3.1 function will have a substantial effect on actin filament dynamics in the AIS. Altering the stability, length, or linearity of the actin filaments building the AIS may then lead to less organized structures (Tojkander et al., 2011).

In addition to actin filament stabilization, Tpm3.1 recruits and activates myosin II (Bryce et al., 2003; Gateva et al., 2017; Meiring et al., 2019), which has recently emerged as an important regulator of AIS structure (Berger et al., 2018; Evans et al., 2017). Recent super-resolution and electron microscopy studies reported a subcellular localization of myosin IIB similar to what we detected for Tpm3.1 (Vassilopoulos et al., 2019; Wang et al., 2020). Myosin II also shows periodicity but not as uniform as actin, and it only partially overlaps with actin rings. Immunogold labeling for pMLC followed by PREM showed gold beads often appearing along filaments perpendicular to actin braids (Vassilopoulos et al., 2019). It is thus plausible that Tpm3.1 further contributes to the structure of the AIS by recruiting myosin II to the fibrillar coat, providing the lattice with contractile characteristics. This is supported by the relatively low myosin IIB immunofluorescence in *Tpm3* KO neurons (Figure 10). However, the reduced myosin IIB expression in Tpm3.1 KO cells is just the first indication of possible interaction of Tpm3.1 and myosin IIB in neurons. Further experiments are required to clarify how Tpm3.1 affects myosin IIB in the AIS. One more alternative explanation for the loss of AIS structure upon Tpm3.1 inhibition could be that Tpm3.1 depletion or inhibition perturbs the specific interactions between Tpm3.1 and proteins contributing to the structure of the AIS; for example, by regulating the binding of βIV-spectrin to the sub-membranous actin rings. Again, further experiments are needed to elucidate which scenario is the correct one.

Tpm3.1 Inhibitors and Genetic Manipulations Affect Actin Filaments via Different Mechanisms

We used here three techniques (small molecule inhibitors, conditional knockout, and shRNA) to perturb Tpm3.1 function or expression. Although the results all point in the same direction, Tpm3.1 inhibitors resulted in a stronger decrease in ankyrin G intensity compared with genetic manipulation. However, there are good reasons for this difference. First, genetic manipulation (conditional knockout and shRNA) decreased Tpm3.1/2 levels but with limited efficacy. This already gives an understandable explanation for the milder effects when protein levels are partially decreased versus an approach where protein function is totally blocked. Furthermore, genetic perturbation and drugs affect filaments differently. Genetic depletion leads to longer-lasting protein level decrease, and loss of a specific filament population can lead to compensating changes. In contrast, the anti-Tpm3.1 drugs do not prevent assembly of Tpm3.1-containing actin filaments (Bonello et al., 2016; Janco et al., 2019). Rather, the drugs incorporate into the Tpm3.1/actin filament and alter the function and stability of the filament (Bonello et al., 2016; Currier et al., 2017; Janco et al., 2019). In addition, their effects are quick, which avoids the likelihood of compensatory changes in the cytoskeleton. Thus, even with 100% knockout efficiency, the drugs are expected to give more penetrant phenotypes than that observed with knockout and shRNA strategies. It is also important to note that, for the main result, we used two structurally distinct Tpm3.1 inhibitors, TR100 and Anisina, and hence, it is highly unlikely to have the same off-target impact.

Tpm3.1 Inhibition Perturbs the Functionality of the AIS

It has been suggested that actin patches are important for cargo transport filtering (Janssen et al., 2017; Leterrier and Dargent, 2014; Watanabe et al., 2012). Tpm3.1 inhibition indeed reduced the number of actin patches in AIS. In contrast, LatB treatment did not decrease the number of patches in the AIS, although it made the AIS leaky. It is possible, however, that LatB affected the turnover and functionality of the actin filaments in patches. Thus, the exact mechanism of how the actin cytoskeleton contributes to the regulation of cargo transport filtering is still unclear.

The effect of Tpm3.1 inhibition by Anisina on firing frequency was relatively rapid (Figure 8) suggesting that the high-order structure of the AIS, which is required for proper functionality of voltage-gated sodium channels is highly sensitive to Tpm3.1 inhibition. Phase-plane plots revealed shallower slopes of action potentials at +20 mV from threshold in Tpm3.1 blocked neurons, compared with control (Figures 8C–8F), thus suggesting more proximal action potential initiation sites (Kress et al., 2008). The result is consistent with our immunofluorescence data showing redistribution and clustering of voltage-gated sodium channels to more somatic location in Tpm3.1-blocked neurons (Figure 7). The finding is also in line with Kress et al. (2008) who showed that a shallower action potential slope is associated with more proximal voltage-gated sodium channel clustering in hippocampal granule cell fibers in comparison with CA3 pyramidal cells having a steeper action potential slope and more distal sodium channel clustering. However, since 15 min Anisina treatment may not have been sufficient to induce marked structural rearrangement of sodium channel localization within the axon, other mechanisms decreasing axonal voltage-gated sodium channel function, such as disruption of sodium channels' order or density at the AIS, may have come to play here. Taken together, Anisina treatment decreases excitability of neurons in a manner consistent with reduced functional sodium channel density at the AIS. Although the mechanistic details await further study, the electrophysiological data give strong functional support to our findings on the redistribution/functional change of sodium channels after Tpm3.1 inhibition.

Taken together, we showed a novel characterization of Tpm3.1 as an AIS component and that its expression and functionality are required for the normal maintenance and functionality of AIS in primary hippocampal neurons.

LIMITATIONS OF THE STUDY

This study was limited to cultured primary hippocampal neurons. In the future, results need to be confirmed in *in vivo* models. It will also be interesting to see whether Tpm3.1 functionality is needed for other cell types. Based on our results, we expect that Tpm3.1-facilitated organization of the AIS is not needed in some neuron types, such as granule cells, where sodium channels are clustered at a different location. Furthermore, for example, Neurofascin depletion has been shown to have different influences in Purkinje cells versus hippocampal neurons (Zonta et al., 2011; Leterrier et al., 2017). Currently, it is unclear whether

different neuron types have different organizations and protein compositions in the AIS, but this is a very interesting study question for the future.

The Tpm3.1 isoform, as most tropomyosin isoforms, is nearly impossible to study without affecting or detecting other tropomyosin isoforms. In this study, conditional knockout was depleting all *Tpm3* gene products and our shRNA was depleting Tpm3.1 and its close homologue Tpm3.2. Antibodies used against Tpm3.1 recognize both Tpm3.1 and Tpm3.2. Genetic depletion of Tpm3.1/2, both with conditional knockout cells (where depletion was induced with Cre infection) and shRNA-induced depletion, was limited. It may indicate that the degradation turnover of Tpm3.1/2 is relatively slow.

METHODS

All methods can be found in the accompanying Transparent Methods supplemental file.

DATA AND CODE AVAILABILITY

Original data have been deposited to Mendeley Data: https://doi.org/10.17632/jw64nf3rn5.1.

SUPPLEMENTAL INFORMATION

Supplemental Information can be found online at https://doi.org/10.1016/j.isci.2020.101053.

AUTHOR CONTRIBUTIONS

A.A. and P.H. designed experiments with the exception of experiments presented in Figures 5, 8, 10, and S6–S8. T.F. designed experiments presented in Figures 5, 10, S7, and S8. C.C.H. designed the experiments presented in Figure S5. T.T. and M.S. designed the experiments presented in Figure 8. A.A. performed all experiments and analyzed all data, with the exception of data and analyses presented in Figures 5B, 8, 10, and S7. H.S. and T.F. performed experiments and analyzed data presented in Figures 5, 10, S7, and S8. T.T. and M.S. performed the experiments and analyzed data presented Figure 8. E.C.H. provided conditional *Tpm3* knockout mice and Figure S6. D.M. assisted with the analysis of the experiments presented in Figures S3 and S5. R.M. assisted with the preparation of neuronal cultures for the experiments performed by A.A. or M.S. L.L. performed co-localization analysis presented in Figure S4. P.W.G. provided tropomyosin constructs, antibody, and inhibitors. C.C.H. provided antibodies for TRIM46, EB1 and NF-186. A.A. and P.H. prepared figures and wrote and edited the manuscript.

DECLARATION OF INTERESTS

The authors declare no competing financial interests except for P.W.G. and E.C.H. who own shares in a company developing anti-tropomyosin drugs.

REFERENCES

Abouelezz, A., Micinski, D., Lipponen, A., and Hotulainen, P. (2019). Sub-membranous actin rings in the axon initial segment are resistant to the action of latrunculin. Biol. Chem. *400*, 1141–1146.

Al-Bassam, S., Xu, M., Wandless, T.J., and Arnold, D.B. (2012). Differential trafficking of transport vesicles contributes to the localization of dendritic proteins. Cell Rep. *2*, 89–100.

Ango, F., di Cristo, G., Higashiyama, H., Bennett, V., Wu, P., and Huang, Z.J. (2004). Ankyrin-based subcellular gradient of neurofascin, an immunoglobulin family protein, directs GABAergic innervation at purkinje axon initial segment. Cell *119*, 257–272.

Bach, C.T., Creed, S., Zhong, J., Mahmassani, M., Schevzov, G., Stehn, J., Cowell, L.N., Naumanen, P., Lappalainen, P., Gunning, P.W., et al. (2009). Tropomyosin isoform expression regulates the transition of adhesions to determine cell speed and direction. Mol. Cell. Biol. *29*, 1506–1514.

Balasanyan, V., Watanabe, K., Dempsey, W.P., Lewis, T.L., Jr., Trinh, L.A., and Arnold, D.B. (2017). Structure and function of an actin-based filter in the proximal axon. Cell Rep. *21*, 2696–2705.

Bennett, V., and Baines, A.J. (2001). Spectrin and ankyrin-based pathways: metazoan inventions for integrating cells into tissues. Physiol. Rev. *81*, 1353–1392.

Berger, S.L., Leo-Macias, A., Yuen, S., Khatri, L., Pfennig, S., Zhang, Y., Agullo-Pascual, E., Caillol, G., Zhu, M.S., Rothenberg, E., et al. (2018). Localized myosin II activity regulates assembly and plasticity of the axon initial segment. Neuron *97*, 555–570.e6.

Bertling, E., and Hotulainen, P. (2017). New waves in dendritic spine actin cytoskeleton: from branches and bundles to rings, from actin binding proteins to post-translational modifications. Mol. Cell Neurosci. *84*, 77–84.

Bonello, T.T., Janco, M., Hook, J., Byun, A., Appaduray, M., Dedova, I., Hitchcock-DeGregori, S., Hardeman, E.C., Stehn, J.R., Bocking, T., et al. (2016). A small molecule inhibitor of tropomyosin dissociates actin binding from tropomyosin-directed regulation of actin dynamics. Sci. Rep. *6*, 19816.

Brachet, A., Leterrier, C., Irondelle, M., Fache, M.P., Racine, V., Sibarita, J.B., Choquet, D., and Dargent, B. (2010). Ankyrin G restricts ion channel diffusion at the axonal initial segment before the establishment of the diffusion barrier. J. Cell Biol. *191*, 383–395.

Broschat, K.O. (1990). Tropomyosin prevents depolymerization of actin filaments from the pointed end. J. Biol. Chem. *265*, 21323–21329.

Bryce, N.S., Schevzov, G., Ferguson, V., Percival, J.M., Lin, J.J., Matsumura, F., Bamburg, J.R., Jeffrey, P.L., Hardeman, E.C., Gunning, P., et al. (2003). Specification of actin filament function and molecular composition by tropomyosin isoforms. Mol. Biol. Cell *14*, 1002–1016.

Clark, K., Sword, B.A., and Dupree, J.L. (2017). Oxidative stress induces disruption of the axon initial segment. ASN Neuro *9*, 1759091417745426.

Creed, S.J., Bryce, N., Naumanen, P., Weinberger, R., Lappalainen, P., Stehn, J., and Gunning, P. (2008). Tropomyosin isoforms define distinct microfilament populations with different drug susceptibility. Eur. J. Cell Biol. *87*, 709–720.

Currier, M.A., Stehn, J.R., Swain, A., Chen, D., Hook, J., Eiffe, E., Heaton, A., Brown, D., Nartker, B.A., Eaves, D.W., et al. (2017). Identification of cancer-targeted tropomyosin inhibitors and their synergy with microtubule drugs. Mol. Cancer Ther. *16*, 1555–1565.

D'Este, E., Kamin, D., Gottfert, F., El-Hady, A., and Hell, S.W. (2015). STED nanoscopy reveals the ubiquity of subcortical cytoskeleton periodicity in living neurons. Cell Rep. *10*, 1246–1251.

Evans, M.D., Tufo, C., Dumitrescu, A.S., and Grubb, M.S. (2017). Myosin II activity is required for structural plasticity at the axon initial segment. Eur. J. Neurosci. *46*, 1751–1757.

Fath, T., Agnes Chan, Y.K., Vrhovski, B., Clarke, H., Curthoys, N., Hook, J., Lemckert, F., Schevzov, G., Tam, P., Watson, C.M., et al. (2010). New aspects of tropomyosin-regulated neuritogenesis revealed by the deletion of Tm5NM1 and 2. Eur. J. Cell Biol. *89*, 489–498.

Fowler, V.M. (2013). The human erythrocyte plasma membrane: a Rosetta Stone for decoding membrane-cytoskeleton structure. Curr. Top. Membr. *72*, 39–88.

Fowler, V.M., and Bennett, V. (1984). Erythrocyte membrane tropomyosin. Purification and properties. J. Biol. Chem. *259*, 5978–5989.

Freal, A., Fassier, C., Le Bras, B., Bullier, E., De Gois, S., Hazan, J., Hoogenraad, C.C., and Couraud, F. (2016). Cooperative interactions between 480 kDa Ankyrin-G and EB proteins assemble the axon initial segment. J. Neurosci. *36*, 4421–4433.

Ganguly, A., Tang, Y., Wang, L., Ladt, K., Loi, J., Dargent, B., Leterrier, C., and Roy, S. (2015). A dynamic formin-dependent deep F-actin network in axons. J. Cell Biol. *210*, 401–417.

Gateva, G., Kremneva, E., Reindl, T., Kotila, T., Kogan, K., Gressin, L., Gunning, P.W., Manstein, D.J., Michelot, A., and Lappalainen, P. (2017). Tropomyosin isoforms specify functionally distinct actin filament populations in vitro. Curr. Biol. *27*, 705–713.

Gray, K.T., Kostyukova, A.S., and Fath, T. (2017). Actin regulation by tropomodulin and tropomyosin in neuronal morphogenesis and function. Mol. Cell Neurosci. *84*, 48–57.

Gunning, P., O'Neill, G., and Hardeman, E. (2008). Tropomyosin-based regulation of the actin cytoskeleton in time and space. Physiol. Rev. *88*, 1–35.

Han, B., Zhou, R., Xia, C., and Zhuang, X. (2017). Structural organization of the actin-spectrin-based membrane skeleton in dendrites and soma of neurons. Proc. Natl. Acad. Sci. U S A *114*, E6678–E6685.

Hannan, A.J., Schevzov, G., Gunning, P., Jeffrey, P.L., and Weinberger, R.P. (1995). Intracellular localization of tropomyosin mRNA and protein is associated with development of neuronal polarity. Mol. Cell Neurosci. *6*, 397–412.

Hedstrom, K.L., Ogawa, Y., and Rasband, M.N. (2008). AnkyrinG is required for maintenance of the axon initial segment and neuronal polarity. J. Cell Biol. *183*, 635–640.

Honkura, N., Matsuzaki, M., Noguchi, J., Ellis-Davies, G.C., and Kasai, H. (2008). The subspine organization of actin fibers regulates the structure and plasticity of dendritic spines. Neuron *57*, 719–729.

Janco, M., Rynkiewicz, M.J., Li, L., Hook, J., Eiffe, E., Ghosh, A., Böcking, T., Lehman, W.J., Hardeman, E.C., and Gunning, P.W. (2019). Molecular integration of the anti-tropomyosin compound ATM-3507 into the coiled coil overlap region of the cancer-associated Tpm3.1. Sci. Rep. *9*, 11262.

Jansen, S., and Goode, B.L. (2019). Tropomyosin isoforms differentially tune actin filament length and disassembly. Mol. Biol. Cell *30*, 671–679.

Janssen, A.F.J., Tas, R.P., van Bergeijk, P., Oost, R., Hoogenraad, C.C., and Kapitein, L.C. (2017). Myosin-V induces cargo immobilization and clustering at the axon initial segment. Front. Cell Neurosci. *11*, 260.

Jenkins, S.M., and Bennett, V. (2001). Ankyrin-G coordinates assembly of the spectrin-based membrane skeleton, voltage-gated sodium channels, and L1 CAMs at Purkinje neuron initial segments. J. Cell Biol. *155*, 739–746.

Jones, S.L., Korobova, F., and Svitkina, T. (2014). Axon initial segment cytoskeleton comprises a multiprotein submembranous coat containing sparse actin filaments. J. Cell Biol. *205*, 67–81.

Kee, A.J., Chagan, J., Chan, J.Y., Bryce, N.S., Lucas, C.A., Zeng, J., Hook, J., Treutlein, H., Laybutt, D.R., Stehn, J.R., et al. (2018). On-target action of anti-tropomyosin drugs regulates glucose metabolism. Sci. Rep. *8*, 4604.

Kee, A.J., Yang, L., Lucas, C.A., Greenberg, M.J., Martel, N., Leong, G.M., Hughes, W.E., Cooney, G.J., James, D.E., Ostap, E.M., et al. (2015). An actin filament population defined by the tropomyosin Tpm3.1 regulates glucose uptake. Traffic *16*, 691–711.

Kis-Bicskei, N., Vig, A., Nyitrai, M., Bugyi, B., and Talian, G.C. (2013). Purification of tropomyosin Br-3 and 5NM1 and characterization of their interactions with actin. Cytoskeleton (Hoboken) *70*, 755–765.

Klinman, E., Tokito, M., and Holzbaur, E.L.F. (2017). CDK5-dependent activation of dynein in the axon initial segment regulates polarized cargo transport in neurons. Traffic *18*, 808–824.

Kole, M.H., Ilschner, S.U., Kampa, B.M., Williams, S.R., Ruben, P.C., and Stuart, G.J. (2008). Action potential generation requires a high sodium channel density in the axon initial segment. Nat. Neurosci. *11*, 178–186.

Kordeli, E., Lambert, S., and Bennett, V. (1995). AnkyrinG. A new ankyrin gene with neural-specific isoforms localized at the axonal initial segment and node of Ranvier. J. Biol. Chem. *270*, 2352–2359.

Koskinen, M., Bertling, E., Hotulainen, R., Tanhuanpaa, K., and Hotulainen, P. (2014). Myosin IIb controls actin dynamics underlying the dendritic spine maturation. Mol. Cell Neurosci. *61*, 56–64.

Koskinen, M., and Hotulainen, P. (2014). Measuring F-actin properties in dendritic spines. Front. Neuroanat. *8*, 74.

Kress, G.J., Dowling, M.J., Meeks, J.P., and Mennerick, S. (2008). High threshold, proximal initiation, and slow conduction velocity of action potentials in dentate granule neuron mossy fibers. J. Neurophysiol. *100*, 281–291.

Kuijpers, M., van de Willige, D., Freal, A., Chazeau, A., Franker, M.A., Hofenk, J., Rodrigues, R.J., Kapitein, L.C., Akhmanova, A., Jaarsma, D., et al. (2016). Dynein regulator NDEL1 controls polarized cargo transport at the axon initial segment. Neuron *89*, 461–471.

Leite, S.C., Sampaio, P., Sousa, V.F., Nogueira-Rodrigues, J., Pinto-Costa, R., Peters, L.L., Brites, P., and Sousa, M.M. (2016). The actin-binding protein alpha-adducin is required for maintaining axon diameter. Cell Rep. *15*, 490–498.

Leite, S.C., and Sousa, M.M. (2016). The neuronal and actin commitment: Why do neurons need rings? Cytoskeleton (Hoboken) *73*, 424–434.

Leterrier, C., Clerc, N., Rueda-Boroni, F., Montersino, A., Dargent, B., and Castets, F. (2017). Ankyrin G membrane partners drive the establishment and maintenance of the axon initial segment. Front. Cell Neurosci. *11*, 6.

Leterrier, C., and Dargent, B. (2014). No Pasaran! Role of the axon initial segment in the regulation of protein transport and the maintenance of axonal identity. Semin. Cell Dev. Biol. *27*, 44–51.

Leterrier, C., Potier, J., Caillol, G., Debarnot, C., Rueda Boroni, F., and Dargent, B. (2015). Nanoscale architecture of the axon initial segment reveals an organized and robust scaffold. Cell Rep. *13*, 2781–2793.

Leterrier, C., Vacher, H., Fache, M.P., d'Ortoli, S.A., Castets, F., Autillo-Touati, A., and Dargent, B. (2011). End-binding proteins EB3 and EB1 link microtubules to ankyrin G in the axon initial segment. Proc. Natl. Acad. Sci. U S A *108*, 8826–8831.

Lewis, T.L., Jr., Mao, T., and Arnold, D.B. (2011). A role for myosin VI in the localization of axonal proteins. PLoS Biol. *9*, e1001021.

Lewis, T.L., Jr., Mao, T., Svoboda, K., and Arnold, D.B. (2009). Myosin-dependent targeting of transmembrane proteins to neuronal dendrites. Nat. Neurosci. *12*, 568–576.

Meiring, J.C.M., Bryce, N.S., Lastra Cagigas, M., Benda, A., Whan, R.M., Ariotti, N., Parton, R.G., Stear, J.H., Hardeman, E.C., and Gunning, P.W. (2019). Colocation of Tpm3.1 and myosin IIa heads defines a discrete subdomain in stress fibres. J. Cell Sci. *132*, 15.

Nakada, C., Ritchie, K., Oba, Y., Nakamura, M., Hotta, Y., Iino, R., Kasai, R.S., Yamaguchi, K., Fujiwara, T., and Kusumi, A. (2003). Accumulation of anchored proteins forms membrane diffusion barriers during neuronal polarization. Nat. Cell Biol. *5*, 626–632.

Pan, Z., Kao, T., Horvath, Z., Lemos, J., Sul, J.Y., Cranstoun, S.D., Bennett, V., Scherer, S.S., and Cooper, E.C. (2006). A common ankyrin-G-based mechanism retains KCNQ and NaV channels at electrically active domains of the axon. J. Neurosci. *26*, 2599–2613.

Papandreou, M.J., and Leterrier, C. (2018). The functional architecture of axonal actin. Mol. Cell Neurosci. *91*, 151–159.

Patterson, G.H., and Lippincott-Schwartz, J. (2002). A photoactivatable GFP for selective photolabeling of proteins and cells. Science *297*, 1873–1877.

Percival, J.M., Thomas, G., Cock, T.A., Gardiner, E.M., Jeffrey, P.L., Lin, J.J., Weinberger, R.P., and Gunning, P. (2000). Sorting of tropomyosin isoforms in synchronised NIH 3T3 fibroblasts: evidence for distinct microfilament populations. Cell Motil. Cytoskeleton *47*, 189–208.

Pleines, I., Woods, J., Chappaz, S., Kew, V., Foad, N., Ballester-Beltran, J., Aurbach, K., Lincetto, C., Lane, R.M., Schevzov, G., et al. (2017). Mutations in tropomyosin 4 underlie a rare form of human macrothrombocytopenia. J. Clin. Invest. *127*, 814–829.

Qu, Y., Hahn, I., Webb, S.E., Pearce, S.P., and Prokop, A. (2017). Periodic actin structures in neuronal axons are required to maintain microtubules. Mol. Biol. Cell *28*, 296–308.

Rasband, M.N. (2010). The axon initial segment and the maintenance of neuronal polarity. Nat. Rev. Neurosci. *11*, 552–562.

Sanchez-Ponce, D., DeFelipe, J., Garrido, J.J., and Munoz, A. (2011). In vitro maturation of the cisternal organelle in the hippocampal neuron's axon initial segment. Mol. Cell Neurosci. *48*, 104–116.

Schafer, D.P., Jha, S., Liu, F., Akella, T., McCullough, L.D., and Rasband, M.N. (2009). Disruption of the axon initial segment cytoskeleton is a new mechanism for neuronal injury. J. Neurosci. *29*, 13242–13254.

Schevzov, G., Bryce, N.S., Almonte-Baldonado, R., Joya, J., Lin, J.J., Hardeman, E., Weinberger, R., and Gunning, P. (2005). Specific features of neuronal size and shape are regulated by tropomyosin isoforms. Mol. Biol. Cell *16*, 3425–3437.

Schevzov, G., Fath, T., Vrhovski, B., Vlahovich, N., Rajan, S., Hook, J., Joya, J.E., Lemckert, F., Puttur, F., Lin, J.J., et al. (2008). Divergent regulation of the sarcomere and the cytoskeleton. J. Biol. Chem. *283*, 275–283.

Song, A.H., Wang, D., Chen, G., Li, Y., Luo, J., Duan, S., and Poo, M.M. (2009). A selective filter for cytoplasmic transport at the axon initial segment. Cell *136*, 1148–1160.

Stehn, J., Mariana, A., Failes, T., Ashokakumar, V., Eiffe, E., Heaton, A., Hook, J., Sivanandhan, D., Arndt, G., Gunning, P., et al. (2016). Synergistic

action of first-in-class anti-tropomyosin compound, ATM-3507 (Anisina) and microtubule targeting inhibitors in pre-clinical models of non-small cell lung cancer (NSCLC). Eur. J. Cancer *69*, S116.

Stefen, H., Hassanzadeh-Barforoushi, A., Brettle, M., Fok, S., Suchowerska, A.K., Tedla, N., Barber, T., Warkiani, M.E., and Fath, T. (2018). A novel microfluidic device-based neurite outgrowth inhibition assay reveals the neurite outgrowth-promoting activity of tropomyosin Tpm3.1 in hippocampal neurons. Cell Mol. Neurobiol. *38*, 1557–1563.

Stehn, J.R., Haass, N.K., Bonello, T., Desouza, M., Kottyan, G., Treutlein, H., Zeng, J., Nascimento, P.R., Sequeira, V.B., Butler, T.L., et al. (2013). A novel class of anticancer compounds targets the actin cytoskeleton in tumor cells. Cancer Res. *73*, 5169–5182.

Sun, X., Wu, Y., Gu, M., Liu, Z., Ma, Y., Li, J., and Zhang, Y. (2014). Selective filtering defect at the axon initial segment in Alzheimer's disease mouse models. Proc. Natl. Acad. Sci. U S A *111*, 14271–14276.

Sung, L.A., Gao, K.M., Yee, L.J., Temm-Grove, C.J., Helfman, D.M., Lin, J.J., and Mehrpouryan, M. (2000). Tropomyosin isoform 5b is expressed in human erythrocytes: implications of tropomodulin-TM5 or tropomodulin-TM5b complexes in the protofilament and hexagonal organization of membrane skeletons. Blood *95*, 1473–1480.

Sung, L.A., and Lin, J.J. (1994). Erythrocyte tropomodulin binds to the N-terminus of hTM5, a tropomyosin isoform encoded by the gamma-tropomyosin gene. Biochem. Biophys. Res. Commun. *201*, 627–634.

Tojkander, S., Gateva, G., Schevzov, G., Hotulainen, P., Naumanen, P., Martin, C., Gunning, P.W., and Lappalainen, P. (2011). A molecular pathway for myosin II recruitment to stress fibers. Curr. Biol. *21*, 539–550.

van Beuningen, S.F., Will, L., Harterink, M., Chazeau, A., van Battum, E.Y., Frias, C.P., Franker, M.A., Katrukha, E.A., Stucchi, R., Vocking, K., et al. (2015). TRIM46 controls neuronal polarity and axon specification by driving the formation of parallel microtubule arrays. Neuron *88*, 1208–1226.

Vassilopoulos, S., Gibaud, S., Jimenez, A., Caillol, G., and Leterrier, C. (2019). Ultrastructure of the axonal periodic scaffold reveals a braid-like organization of actin rings. Nat. Commun. *10*, 5803.

Vindin, H., and Gunning, P. (2013). Cytoskeletal tropomyosins: choreographers of actin filament functional diversity. J. Muscle Res. Cell Motil. *34*, 261–274.

Wang, T., Li, W., Martin, S., Papadopulos, A., Shamsollahi, G., Lanoue, V., Padmanabhan, P., Huang, H., Yu, X., Anggono, V., et al. (2020). Actomyosin-II facilitates long-range retrograde transport of large cargoes by controlling axonal radial contractility. J. Cell Biol. *219*, e201902001.

Watanabe, K., Al-Bassam, S., Miyazaki, Y., Wandless, T.J., Webster, P., and Arnold, D.B. (2012). Networks of polarized actin filaments in the axon initial segment provide a mechanism for

sorting axonal and dendritic proteins. Cell Rep. *2*, 1546–1553.

Weber, A., Pennise, C.R., Babcock, G.G., and Fowler, V.M. (1994). Tropomodulin caps the pointed ends of actin filaments. J. Cell Biol. *127*, 1627–1635.

Weinberger, R., Schevzov, G., Jeffrey, P., Gordon, K., Hill, M., and Gunning, P. (1996). The molecular composition of neuronal microfilaments is spatially and temporally regulated. J. Neurosci. *16*, 238–252.

Winckler, B., Forscher, P., and Mellman, I. (1999). A diffusion barrier maintains distribution of membrane proteins in polarized neurons. Nature *397*, 698–701.

Xu, K., Zhong, G., and Zhuang, X. (2013). Actin, spectrin, and associated proteins form a periodic cytoskeletal structure in axons. Science *339*, 452–456.

Xu, X., and Shrager, P. (2005). Dependence of axon initial segment formation on Na+ channel expression. J. Neurosci. Res. *79*, 428–441.

Yamashiro, S., Gokhin, D.S., Sui, Z., Bergeron, S.E., Rubenstein, P.A., and Fowler, V.M. (2014). Differential actin-regulatory activities of Tropomodulin1 and Tropomodulin3 with diverse tropomyosin and actin isoforms. J. Biol. Chem. *289*, 11616–11629.

Yang, Y., Ogawa, Y., Hedstrom, K.L., and Rasband, M.N. (2007). βIV spectrin is recruited to axon initial segments and nodes of Ranvier by ankyrinG. J. Cell Biol. *176*, 509–519.

Zhong, G., He, J., Zhou, R., Lorenzo, D., Babcock, H.P., Bennett, V., and Zhuang, X. (2014). Developmental mechanism of the periodic membrane skeleton in axons. Elife *3*, e04581.

Zhou, D., Lambert, S., Malen, P.L., Carpenter, S., Boland, L.M., and Bennett, V. (1998). AnkyrinG is required for clustering of voltage-gated Na channels at axon initial segments and for normal action potential firing. J. Cell Biol. *143*, 1295–1304.

Zonta, B., Desmazieres, A., Rinaldi, A., Tait, S., Sherman, D.L., Nolan, M.F., and Brophy, P.J. (2011). A critical role for Neurofascin in regulating action potential initiation through maintenance of the axon initial segment. Neuron *69*, 945–956.

Supplemental Information

Tropomyosin Tpm3.1 Is Required to Maintain

the Structure and Function

of the Axon Initial Segment

Amr Abouelezz, Holly Stefen, Mikael Segerstråle, David Micinski, Rimante Minkeviciene, Lauri Lahti, Edna C. Hardeman, Peter W. Gunning, Casper C. Hoogenraad, Tomi Taira, Thomas Fath, and Pirta Hotulainen
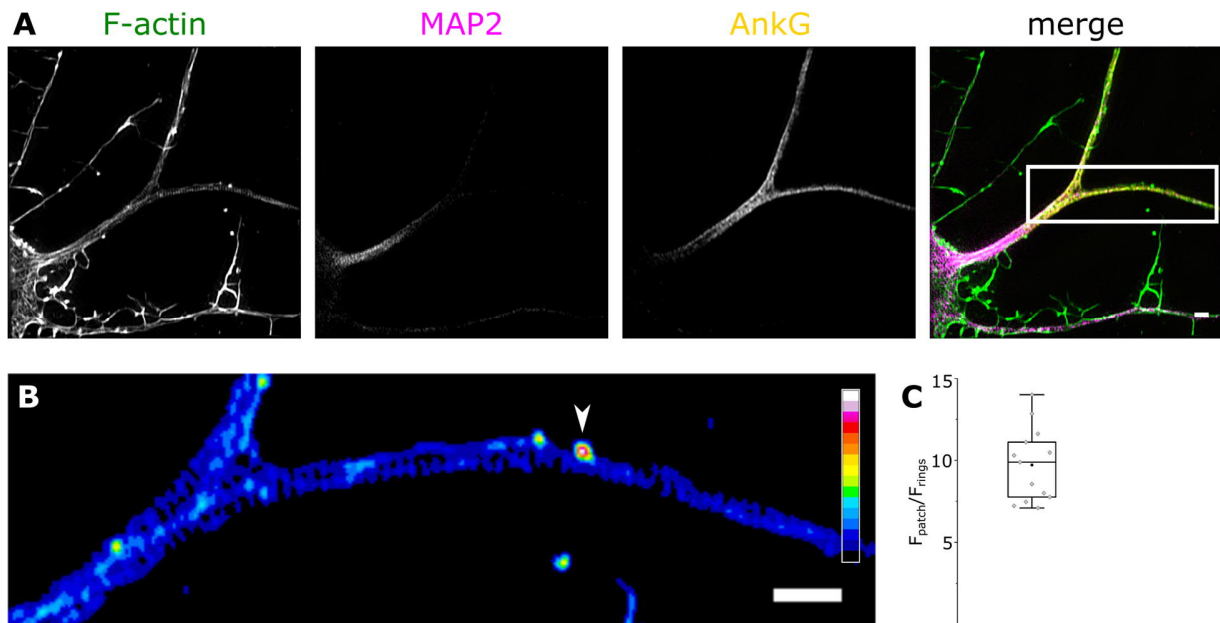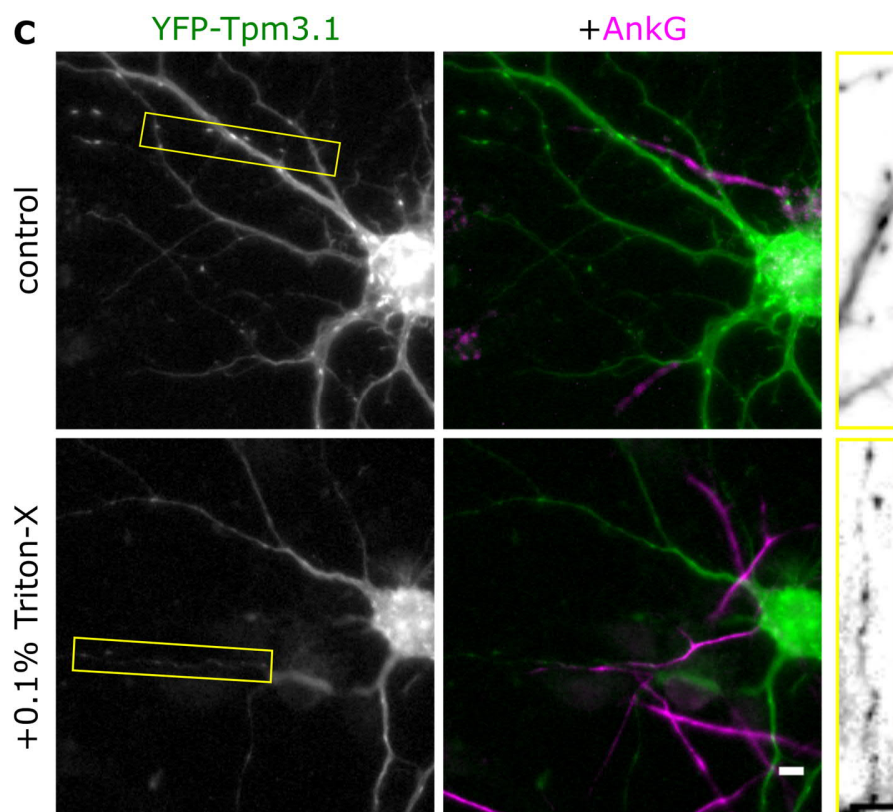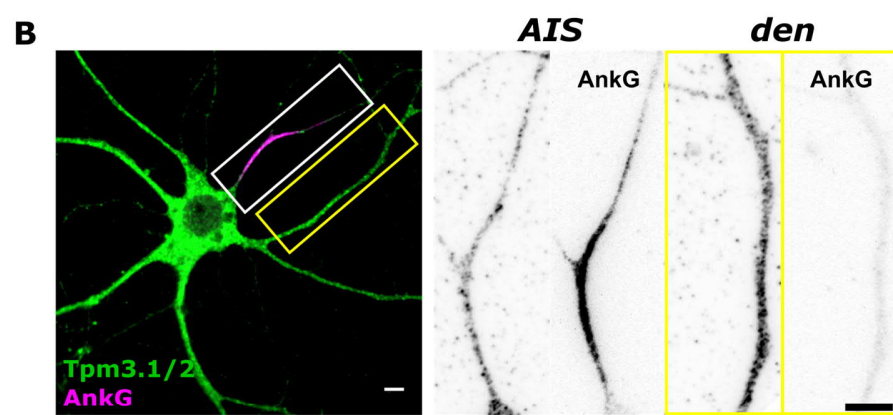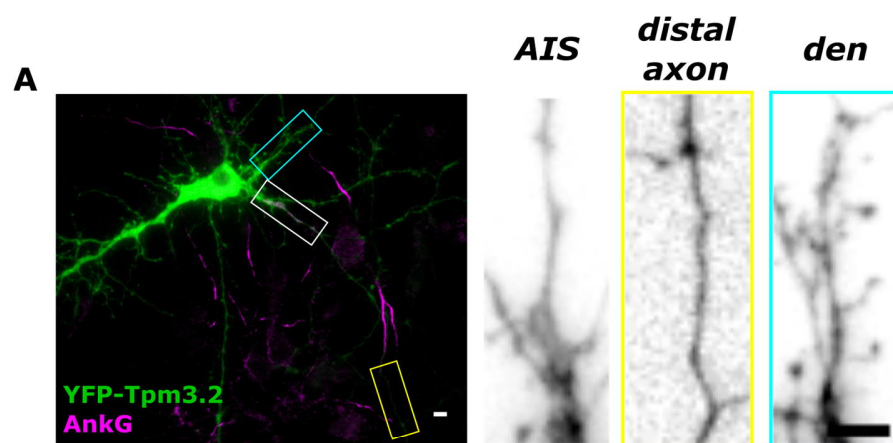
Supplementary figure 1 (related to Figure 1) | AIS actin patches contain more F-actin than sub-membranous actin rings.

(A) SIM reconstructions of rat hippocampal neuron at 14 DIV stained using Alexa 488-tagged phalloidin, anti-MAP2, and anti-ankyrin G. The boxed region is enlarged in (B).

(B) Maximum intensity projection of a SIM reconstruction of F-actin in the boxed region, corresponding to the AIS. Color code indicates normalized fluorescence intensity levels. Arrowhead indicates F-actin patch.

(C) The median fluorescence intensity of phalloidin in AIS actin patches was, on average, 9.7 times that of sub-membranous actin rings. Black circle represents mean value. Box borders represent the 25th and 75th percentiles, whiskers represent minimum and maximum values less than 1.5x the interquartile range lower or higher than the 25th or 75th percentiles, respectively (Tukey style). n = 13, 4 independent experiments, same data set used in Fig. 9. Scale bar: 1 μm.

A

AIS   *distal axon*   *den*

YFP-Tpm3.2
AnkG

B

AIS   *den*

AnkG   AnkG

Tpm3.1/2
AnkG

C   YFP-Tpm3.1   +AnkG
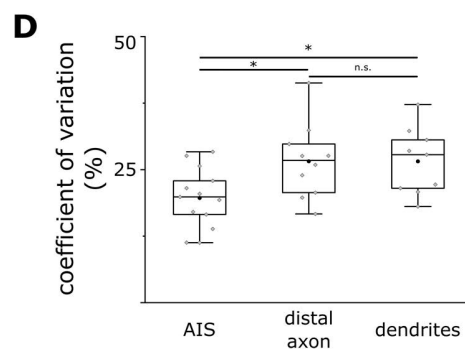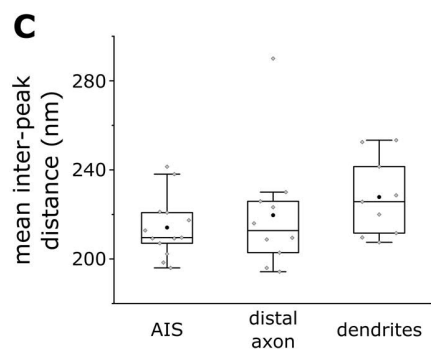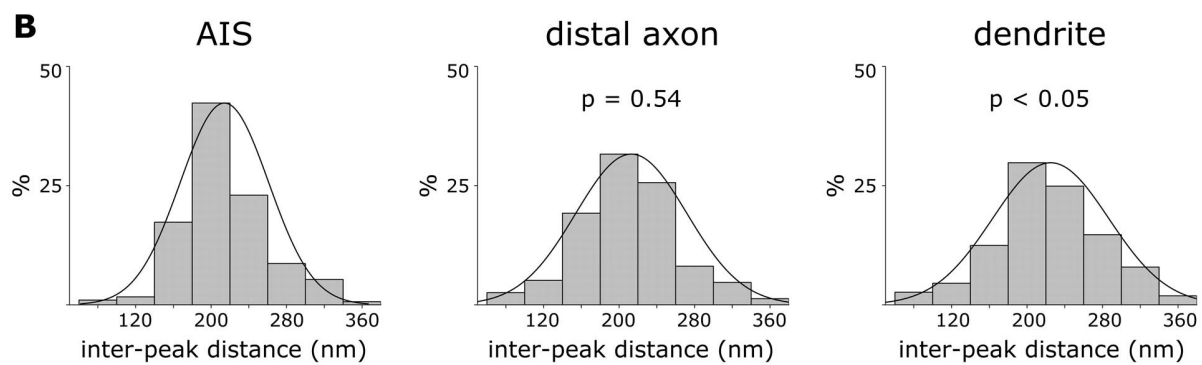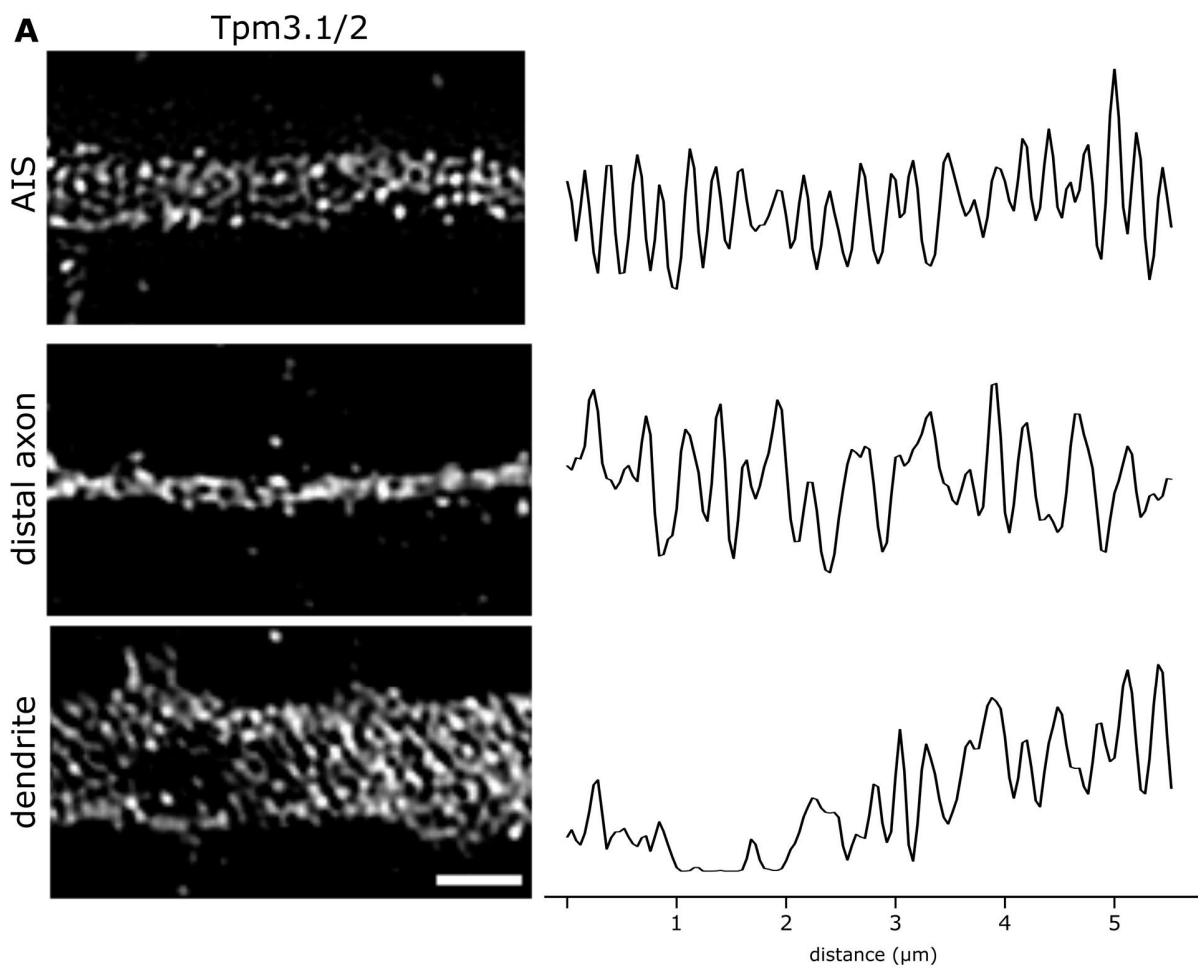
control

+0.1% Triton-X

Supplementary figure 2 (related to Figure 2) | Tpm3.1 shows a non-uniform distribution similar to AIS actin patches.

(A) Rat hippocampal neurons expressing YFP-Tpm3.2. Neurons were fixed 8 hours post-transfection. Anti-ankyrin G served to label the AIS. Compared to YFP-Tpm3.1, YFP-Tpm3.2 shows a diffuse staining in the AIS (white box) and distal regions of the axon (yellow box), and a much stronger presence in the somatodendritic compartment (cyan box) and dendritic spines. Scale bar: 10 µm.

(B) Tpm3.1 was visualized in rat hippocampal neurons at 10 DIV using anti-γ/9d. Anti-ankyrin G served to label the AIS. Anti-γ/9d simultaneously detects Tpm3.1 and Tpm3.2. Anti-γ/9d immunofluorescence in the AIS was unevenly distributed in the AIS, with patches of high intensity similar to AIS actin patches. In contrast, anti-γ/9d in the somatodendritic domain was diffuse and ubiquitous. Scale bar: 5 µm.

(C) Rat hippocampal neurons expressing YFP-Tpm3.1 were either fixed or extracted in 0.1% Triton-X for 60 seconds then fixed 8 hours post-transfection. Anti-ankyrin G served to label the AIS. Patches of YFP-Tpm3.1 can still be seen in the AIS after detergent extraction. Scale bar: 5 µm.

A Tpm3.1/2

AIS

distal axon

dendrite

distance (μm)

B

AIS

distal axon

p = 0.54

dendrite

p < 0.05

inter-peak distance (nm)

C

D

Supplementary figure 3 (related to Figure 3) | Tpm3.1 does not exhibit clear periodicity in the distal axon or in dendrites of cultured rat hippocampal neurons.

(A) *Left*: SIM reconstructions of the AIS, a distal region of the axon, and a dendrite of a rat hippocampal neuron at 14 DIV stained using anti-γ/9d. Periodic Tpm3.1/2 immunofluorescence is visible in the AIS, but not in the distal regions of the axon or in dendrites. *Right*: Anti-γ/9d fluorescence intensity profiles from the corresponding images. Scale bar: 1 μm.

(B) Distance between individual peaks in normalized Tpm3.1 fluorescence intensity profiles. In the AIS, 42.3% of the peaks were separated by 200 nm. In distal axons and dendrites, the corresponding values were 31.6% and 29.8%, respectively. The inter-peak distances in distal axons were not significantly different compared to the AIS, while in dendrites the distribution was significantly different (Kolmogorov-Smirnov test).

(C and D) The mean inter-peak distance (C) for individual cells at the AIS, distal axon, or dendrites was not significantly different (ANOVA), while the coefficients of variation (D) were higher in the distal axon and dendrites compared to the AIS ($p < 0.05$, ANOVA, Tukey's test). Box borders represent the 25th and 75th percentiles, whiskers represent minimum and maximum values less than 1.5x the interquartile range lower or higher than the 25th or 75th percentiles, respectively (Tukey style). * denotes statistical significance. *: p < 0.05.
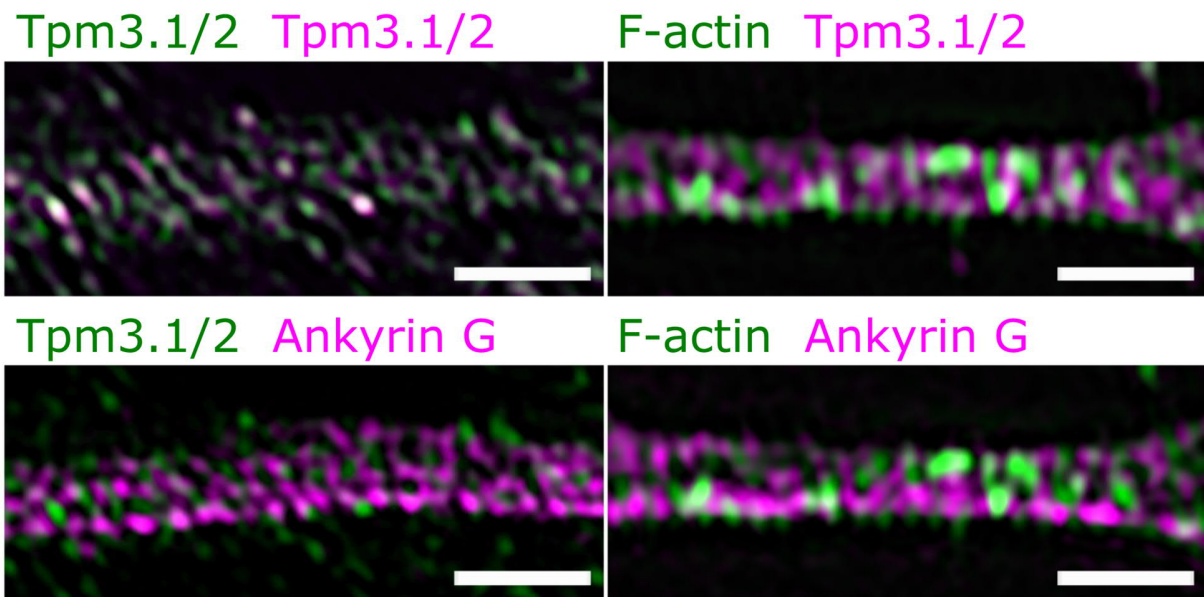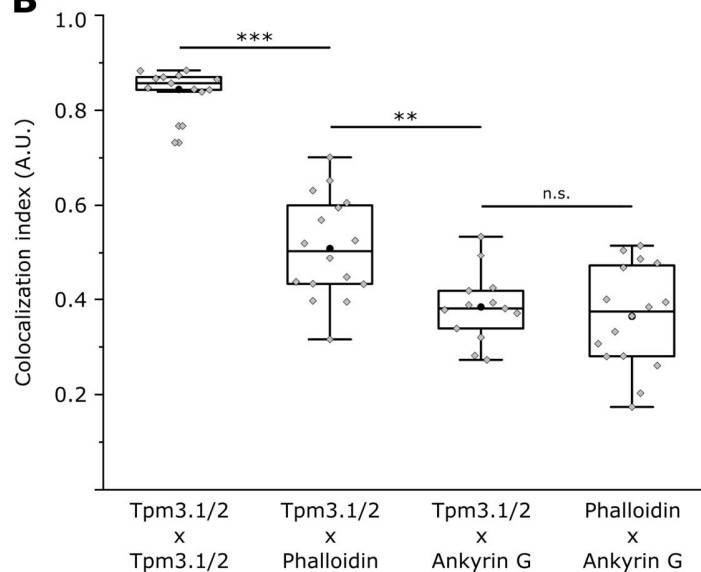
Supplementary figure 4 (related to Figure 3) | F-actin and Tpm3.1 exhibit partial overlap.

(A) SIM reconstruction of the AIS of a rat hippocampal neuron at 14 DIV labelled using anti-γ/9d and phalloidin to visualize Tpm3.1 and F-actin, respectively. *Left:* cells were stained using two different secondary antibodies, Alexa-488 and 647-tagged, to detect anti-γ/9d. *Right:* Cells were stained using Alexa 488-tagged phalloidin and anti-γ/9d followed by an Alexa 647-tagged secondary antibody. Anti-Ankyrin G served to label the AIS. Ankyrin G labeling was used as a negative control (F-actin and ankyrin G show complementary distribution) in co-localization analysis. Scale bar: 1 μm.

(B) The double-labelled Tpm3.1 showed a Pearson's coefficient of colocalization (PCC) of 0.84 ± 0.01 (mean ± SEM), while the negative control (phalloidin x ankyrin G) showed a PCC of 0.36 ± 0.03. Tpm3.1 x ankyrin G showed a similar PCC (0.38 ± 0.02) to the negative control, suggesting that Tpm3.1/2 and ankyrin G have complementary localization. Tpm3.1/2 x phalloidin showed partial co-localization, with a significantly different co-localization index of 0.51 ± 0.03 compared to both positive and negative controls (ANOVA, Tukey's test). Black circle represents mean value. Box borders represent the 25th and 75th percentiles, whiskers represent minimum and maximum values less than 1.5x the interquartile range lower or higher than the 25th or 75th percentiles, respectively (Tukey style). Neurons double-labelled with Tpm3.1/2 and ankyrin G: n = 13, Neurons labeled with phalloidin, ankyrin G and Tpm3.1/2: n = 16. * denotes statistical significance. **: p < 0.01; ***: p < 0.001.
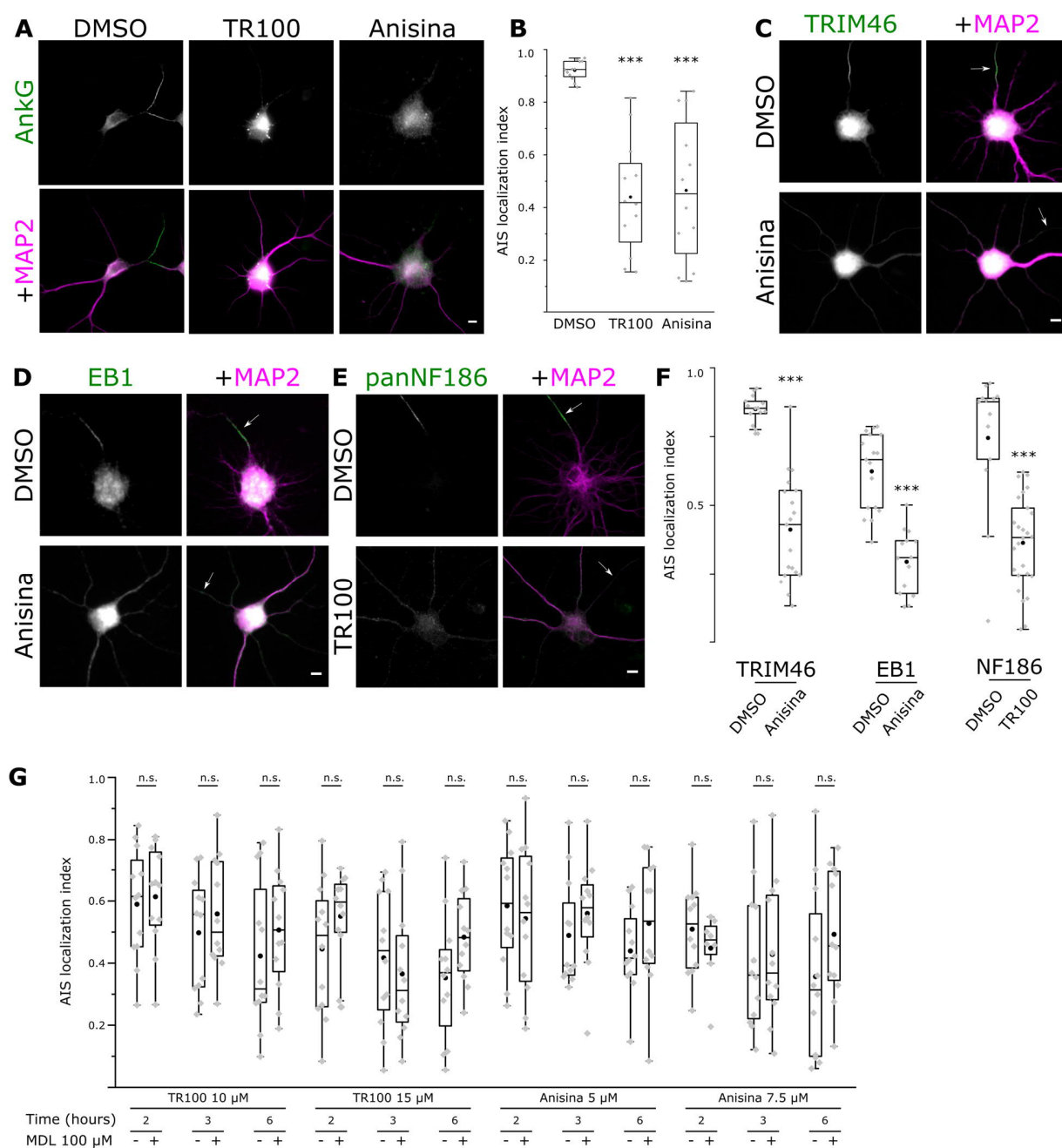
Supplementary figure 5 (related to Figure 4) | Overnight inhibition of Tpm3.1 reduces the accumulation of ankyrin G and other AIS markers at the AIS.

(A) Rat hippocampal neurons treated overnight at 9 DIV using DMSO or the small-molecule Tpm3.1 inhibitors TR100 or Anisina (ATM3507). Anti-MAP2 served to label the somatodendritic domain, anti-ankyrin G served to measure the accumulation of ankyrin G.
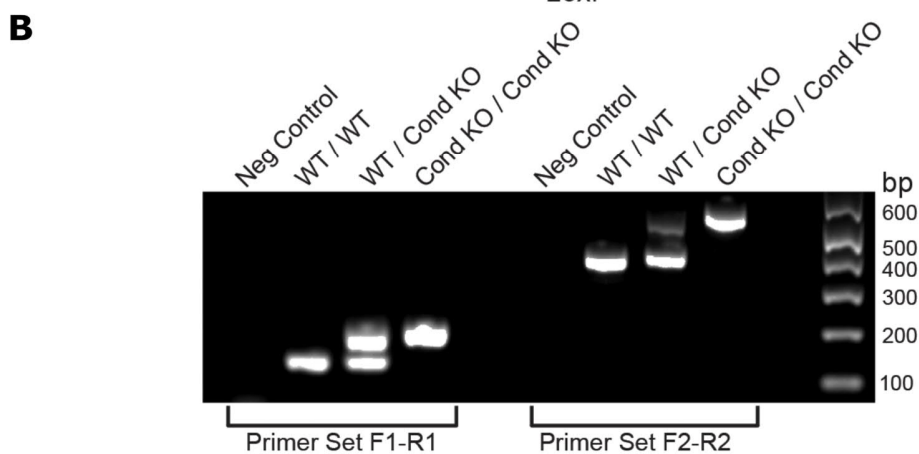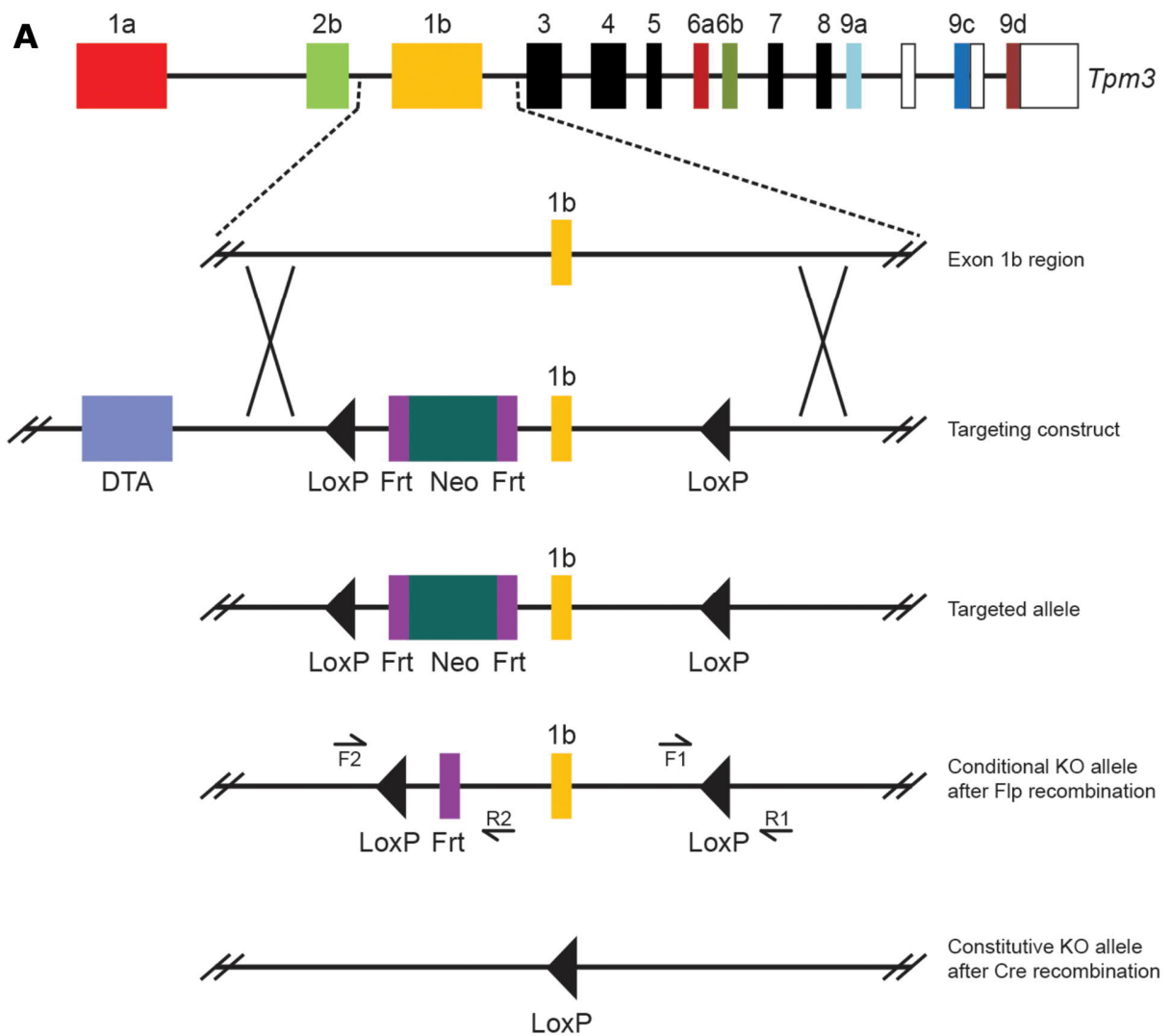
(B) AIS localization indices for neurons treated using DMSO, TR100 (5 µM), or Anisina (2.5 µM). Both TR100- (mean ALI: 0.44 ± 0.06, mean $\pm$ SEM) and Anisina-treated neurons (mean ALI: 0.48 ± 0.09, mean

± SEM) were significantly different from DMSO controls (mean ALI: 0.92 ± 0.01, mean ± SEM; Mann-Whitney *U* test). Black circles represent mean values. For each treatment: n = 12, 3 independent experiments. Scale bar: 5 µm.

(C, D, and E) Rat hippocampal neurons treated at 9-11 DIV using, Anisina (5 µM for 6 hours), TR100 (5 µM overnight), or equivalent volumes of DMSO. Anti-MAP2 served to label the somatodendritic domain. Anti-TRIM46 (C), anti-EB1 (D), or panNF-186 (E) served to visualize the corresponding AIS marker. DMSO-treated neurons showed typical accumulation of TRIM46 and EB1, which are implicated in the regulation of microtubules, as well as the AIS-specific adhesion protein neurofascin-186 (NF-186). Anisina- or TR100-treated neurons showed no accumulation of any of these proteins at the AIS. Scale bar: 5 µm.

(F) AIS localization indices for anti-TRIM46, anti-EB1- or anti-NF186. The ALI was significantly lower in all Anisina- or TR100-treated neurons: TRIM46; DMSO: 0.84 ± 0.01, mean ± SEM, n = 14, 3 independent experiments, Anisina: 0.41 ± 0.04, mean ± SEM, n = 19, 3 independent experiments, p < 0.001, *t*-test; EB1; DMSO: 0.62 ± 0.03, mean ± SEM, n = 17, 3 independent experiments, Anisina: 0.29 ± 0.03, mean ± SEM, n = 14, 3 independent experiments, p < 0.001, *t*-test; NF-186; DMSO: 0.75 ± 0.07, mean ± SEM, n = 13, 3 independent experiments, TR100: 0.36 ± 0.03, mean ± SEM, n = 26, 3 independent experiments, p < 0.001, *t*-test.

(G) AIS localization indices (ALI) for ankyrin G in rat hippocampal neurons treated at 10 DIV using the small-molecule Tpm3.1 inhibitors TR100 or Anisina (ATM3507) for 2, 3, or 6 hours, in the presence or absence of the calpain inhibitor MDL28170 (100 µM). The presence of MDL28170 did not significantly affect the ALI for any of the treatments (Mann-Whitney *U* test). Anisina 7.5 µM + MDL28170 100 µM, 2 hours: n = 8, 2 independent experiments; all other treatments: n = 12, 3 independent experiments. Part of these data were used for Figure 4. Black circles represent mean value. Box borders represent the 25th and 75th percentiles, whiskers represent minimum and maximum values less than 1.5x the interquartile range lower or higher than the 25th or 75th percentiles, respectively (Tukey style). * denotes significance. ***: p < 0.001; n.s.: not significant.

A

1a | 2b | 1b | 3 | 4 | 5 | 6a 6b | 7 | 8 | 9a | | 9c | 9d | *Tpm3*

Exon 1b region

Targeting construct

DTA | LoxP | Frt | Neo | Frt | 1b | LoxP

Targeted allele

LoxP | Frt | Neo | Frt | 1b | LoxP

Conditional KO allele after Flp recombination

F2 | LoxP | Frt | R2 | 1b | F1 | LoxP | R1

Constitutive KO allele after Cre recombination

LoxP

B

Neg Control | WT / WT | WT / Cond KO | Cond KO / Cond KO | Neg Control | WT / WT | WT / Cond KO | Cond KO / Cond KO

bp
600
500
400
300
200
100

Primer Set F1-R1 | Primer Set F2-R2

Supplementary figure 6 (related to Figure 5) | Generation of the Tpm3 gene exon 1b knockout mouse.

(A) Genomic fragments of the Exon 1b region were assembled into a targeting vector containing a Neo cassette flanked by Frt sites located upstream of exon 1b. LoxP sites were inserted upstream of the Neo cassette and in the 3' region downstream from exon 1b. A diphtheria toxin A (DTA) cassette was used in the targeting construct for negative selection. ES cells were electroporated with the targeting construct and the selected ES cell clones were microinjected into C57Bl/6 blastocysts to generate chimeras containing the targeted allele. Chimeric mice were subsequently bred against Flp transgenic mice to remove the Neo drug selection cassette via Flp-mediated recombination and obtain germline F1 mutants with the conditional knockout allele. The location of the PCR genotyping primer pairs is indicated (arrows, F1-R1 and F2-R2). Exon 1b can be excised to create the constitutive full knockout allele by Cre-mediated recombination of the LoxP sites in the conditional knockout allele.

(B) PCR genotyping of the conditional knockout allele prior to Cre-mediated recombination. Primer set 1: The wild type (WT) allele is 151 bp and the conditional knockout (Cond KO) allele is 212 bp. Primer Set 2: The wild type (WT) allele is 402 bp and the conditional knockout (Cond KO) allele is 536 bp. A negative (Neg) control for each primer set containing no template DNA is also shown. For heterozygous mice (WT/CondKO) the bands generated by the F2-R2 primer set favored the smaller sized band in abundance; whereas a more even distribution was seen with the bands generated by the F1-R1 primer set.
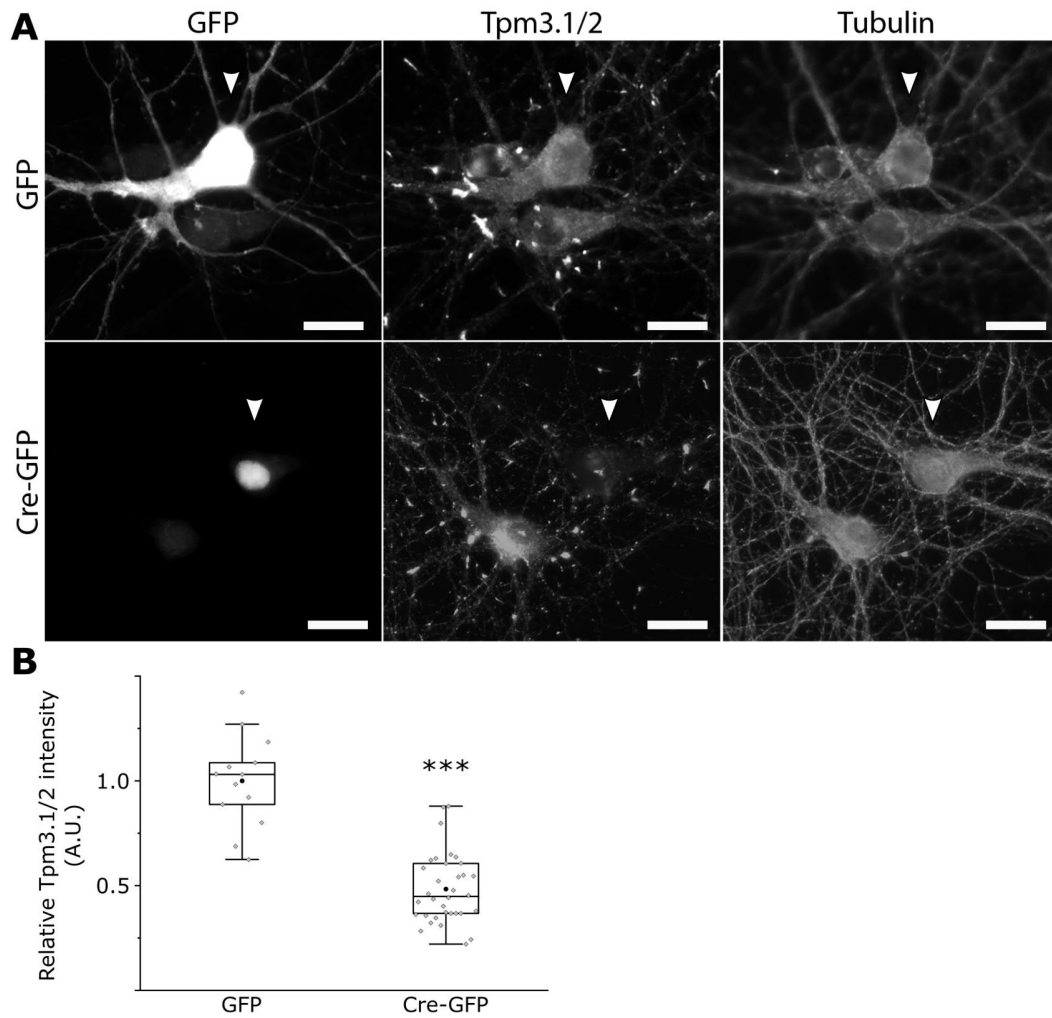
Supplementary figure 7 (related to Figure 5) | Validation of the reduction of Tpm3 protein levels.

(A) Tpm3.1/2 immunofluorescence in cultured hippocampal neurons of Tpm3 conditional knockout mice. Arrowheads indicate a neuron expressing either GFP or GFP-tagged Cre-recombinase (Cre-GFP). Scale bars: 20 μm.

(B) Normalized relative intensity of anti-2G10.2 fluorescence in the somata of neurons expressing GFP or Cre-GFP (Ratios for GFP or Cre-GFP expressing neurons relative to control neurons in the same picture, normalized to mean GFP ratio: GFP, 1.00 ± 0.06, mean ± SEM; Cre-GFP, 0.48 ± 0.03, p < 0.001, *t*-test). Black circles represent mean value. Box borders represent the 25th and 75th percentiles, whiskers represent minimum and maximum values less than 1.5x the interquartile range lower or higher than the 25th or 75th percentiles, respectively (Tukey style). GFP-infected: n = 13 pictures (ratios), 13 GFP-expressing cells, 21 controls; Cre-GFP infected: n = 34 pictures (ratios), 36 Cre-GFP expressing neurons, 55 controls. * denotes statistical significance. ***: p < 0.001.
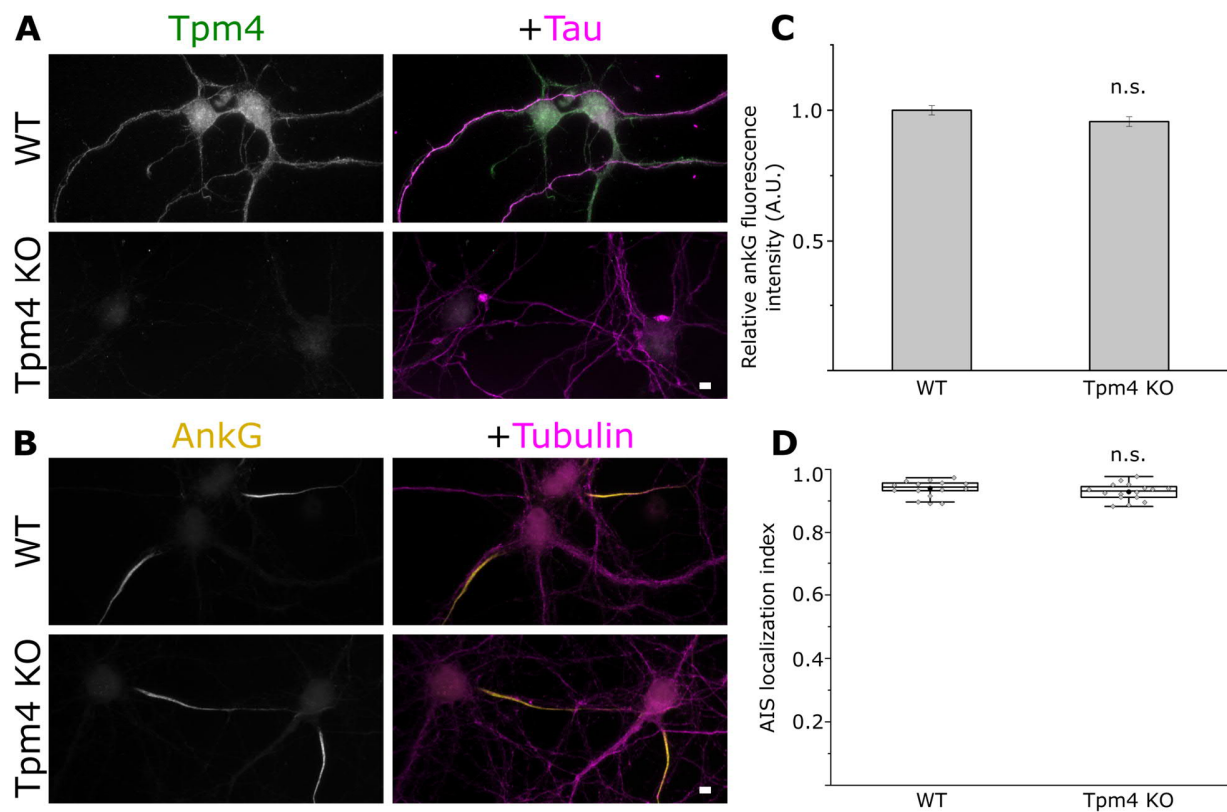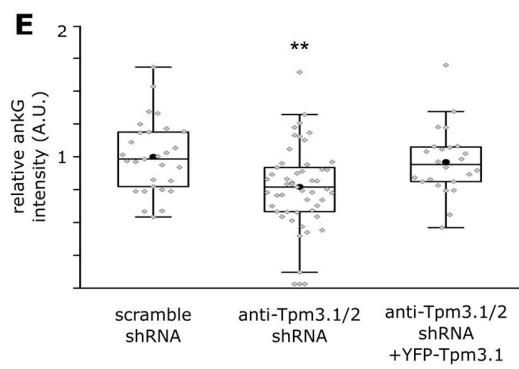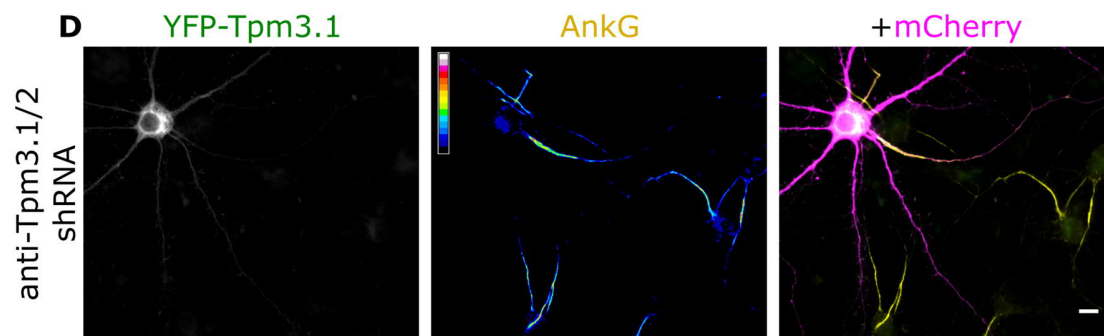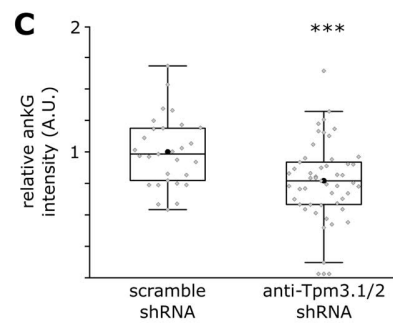
Supplementary figure 8 (related to Figure 5) | *Tpm4* knockout mice show typical accumulation of ankyrin G at the AIS.

(A) Cultured hippocampal neurons of wild-type and *Tpm4* knockout mice showing the absence of Tpm4 immunofluorescence in the knockouts. Anti-Tau served to label axons.

(B) *Tpm4* knockout mice show typical accumulation of ankyrin G. β3-tubulin served to label neurons. Scale bars: 5 μm.

(C) The difference in the mean AIS ankyrin G fluorescence intensity between wild-type (1 ± 0.02, mean ± SEM) and knock-out (0.96 ± 0.02, mean ± SEM) neurons was not statistically significant (Mann-Whitney *U* test). Wild-type: n = 122, 3 independent experiments; *Tpm4* knockout: n = 147, 3 independent experiments. Error bars represent standard error of mean.

(D) AIS localization indices (ALI) did not differ between WT and Tpm4 KO neurons (*t*-test, WT: 0.94 ± 0.01, mean ± SEM, n = 14, 2 independent experiments; Tpm4 KO: 0.93 ± 0.01, mean ± SEM, n = 16, 2 independent experiments). Black circles represent mean values. Box borders represent the 25th and 75th percentiles, whiskers represent minimum and maximum values less than 1.5x the interquartile range lower or higher than the 25th or 75th percentiles, respectively (Tukey style). n.s.: not significant.

A

Tpm3.1/2   AnkG   +mCherry

scramble shRNA

anti-Tpm3.1/2 shRNA

B

relative Tpm3.1/2 intensity (A.U.)

***

scramble shRNA   anti-Tpm3.1/2 shRNA

C

relative ankG intensity (A.U.)

***

scramble shRNA   anti-Tpm3.1/2 shRNA

D

YFP-Tpm3.1   AnkG   +mCherry

anti-Tpm3.1/2 shRNA

E

relative ankG intensity (A.U.)

**

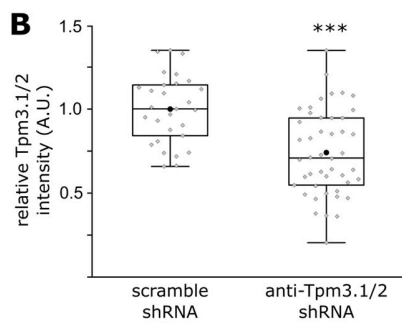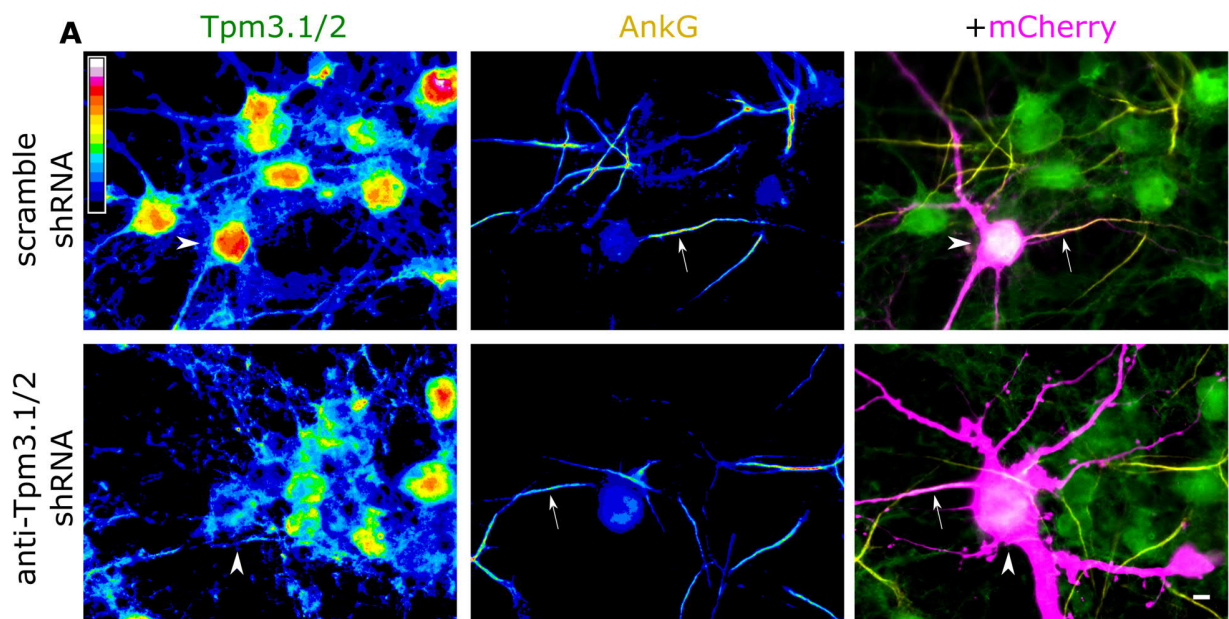scramble shRNA   anti-Tpm3.1/2 shRNA   anti-Tpm3.1/2 shRNA +YFP-Tpm3.1

Supplementary figure 9 (related to Figure 5) | Tpm3.1/2 knockdown reduces the accumulation of ankyrin G at the AIS.

(A) Rat hippocampal neurons transfected at 10 DIV using either anti-Tpm3.1/2 or scramble shRNA, and neighboring, non-transfected neurons. Neurons were fixed at 14 DIV and stained using anti-γ/9d and anti-ankyrin G. Arrowheads point to the transfected neuron, arrows point to axons of transfected neurons. Color code indicates normalized fluorescence intensity levels. Scale bar: 5 μm.

(B) Normalized relative intensity of anti-γ/9d fluorescence in the somata of neurons expressing scramble or anti-Tpm3.1/2 shRNA (scramble shRNA: 1 ± 0.04, mean ± SEM; shRNA: 0.74 ± 0.04, mean ± SEM, p < 0.001, *t* test).

(C) Relative anti-ankyrin G fluorescence intensity in in each group (scramble shRNA: 1 ± 0.05, mean ± SEM; shRNA: 0.77 ± 0.04, mean ± SEM, p < 0.01, *t* test). Scramble shRNA: n = 29, 3 independent experiments; anti-Tpm3.1/2 shRNA: n = 51, 3 independent experiments.

(D) Rat hippocampal neurons expressing mCherry-tagged anti-Tpm3.1/2 shRNA and YFP-tagged human Tpm3.1 at 10-14 DIV. Human Tpm3.1 differs from rat Tpm3.1 in the sequence within the targeted region. Anti-ankyrin G served to visualize ankyrin G. A neuron expressing YFP-Tpm3.1 and anti-Tpm3.1/2 shRNA showing typical ankyrin G accumulation at the AIS. Color code indicates normalized fluorescence intensity levels.

(E) Relative anti-ankyrin G fluorescence intensity in in each group (scramble shRNA: 1 ± 0.05, mean ± SEM; shRNA: 0.77 ± 0.04, mean ± SEM; anti-Tpm3.1/2 shRNA + YFP-Tpm3.1: 0.96 ± 0.05, mean ± SEM; p < 0.01, ANOVA, Tukey's test). Anti-Tpm3.1 shRNA: n = 42, 2 independent experiments, partially used for (B) and (C); scramble shRNA: n = 28, 2 independent experiments, partially used for (B) and (C); anti-Tpm3.1/2 shRNA + YFP-Tpm3.1: n = 26, 2 independent experiments. Black circles represent mean value. Box borders represent the 25th and 75th percentiles, whiskers represent minimum and maximum values less than 1.5x the interquartile range lower or higher than the 25th or 75th percentiles, respectively (Tukey style). * denotes statistical significance. **: p < 0.01; ***: p < 0.001. Scale bar: 5 μm.
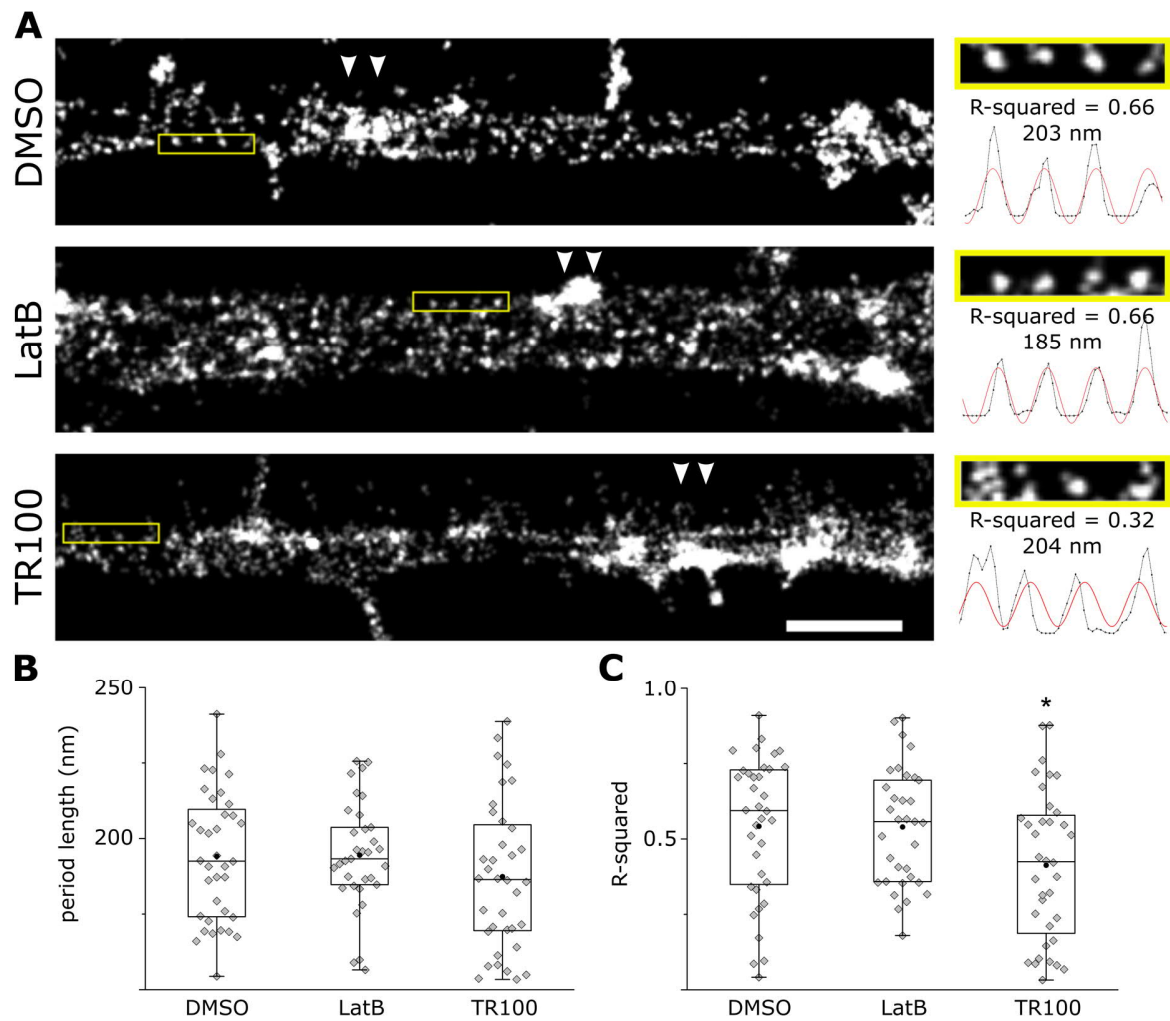
Supplementary figure 10 (related to Figure 9) | The periodicity of actin rings in the AIS is disrupted upon Tpm3.1 inhibition, but not latrunculin-B treatment.

(A) *Left*: STORM reconstructions of the AIS of rat hippocampal neurons at 14 DIV, treated overnight using either DMSO (0.2%), LatB (5 μM), or TR100 (5 μM). Alexa 647-tagged phalloidin served to label F-actin. Arrowheads point to AIS actin patches. *Right*: Higher magnification of the yellow-boxed area. The intensity profiles (black lines) and the best Fourier series fit (red lines) are shown. The period lengths and the R-squared values of the fits are indicated. 3 profiles were plotted in every neuron where periodicity was best visible.

(B) Period lengths in each group. The difference in mean period length between groups was not statistically significant (ANOVA).

(C) R-squared values of individual Fourier series fits in each group. TR100-treated neurons showed a significantly lower R-squared value, indicating a poorer Fourier series fit. LatB-treated neurons were not different from DMSO controls (Mann-Whitney *U* test). Black circles represent mean value. Box borders

represent the 25th and 75th percentiles, whiskers represent minimum and maximum values less than 1.5x the interquartile range lower or higher than the 25th or 75th percentiles, respectively (Tukey style). DMSO: n = 12 neurons, 5 independent experiments; LatB: n = 11 neurons, 4 independent experiments; TR100: n = 12 neurons, 4 independent experiments. * denotes statistical significance. *: p < 0.05. Scale bar: 1 μm.

TRANSPARENT METHODS

Neuronal cultures, transfections, and preparation of fixed samples

Neuronal cultures were prepared as described previously (Hotulainen et al., 2009). We collected brains from embryonic day 17 Wistar rat fetuses of either sex, removed the meninges, dissected the hippocampi, and dissociated cells in 0.05% papain. Next, we mechanically triturated and suspended the cells in Ca^{2+}- and Mg^{2+}-free HBBS medium containing sodium pyruvate (1 mM), HEPES (10 mM, pH 7.2), and DNase I (20 U/ml, Sigma-Aldrich). We plated the cells in 24-well plates on glass coverslips 13-mm in diameter coated using poly-L-lysine (0.01 mg/ml, Sigma-Aldrich) in Neurobasal medium (Invitrogen) supplemented with B-27 (Invitrogen), L-glutamine (Invitrogen), and primocin (InvivoGen). For SIM experiments, we used square high-performance glass coverslips 18 x 18 mm (Zeiss) in 6-well cell culture plates. For STORM experiments, we used glass-bottomed 35 mm dishes (Mattek). For experiments involving transfections, we plated neurons at a density of 75,000 cells/cm^2. For all other experiments, we plated 3,500 cells/cm^2. We cultured the neurons in a humidified incubator at 37°C and 5% CO_2, and refreshed the media twice weekly at regular intervals. We used Lipofectamine 2000 (Invitrogen) to transfect 8-10 DIV neurons as described previously (Hotulainen et al., 2009). We used 4% PFA in PBS for 10-15 minutes at room temperature to fix neurons in preparation for immunofluorescence. For the extraction of soluble proteins (Supplementary figure 5) we treated neurons using 0.1% Triton-X in cytoskeleton buffer (10 mM MES, 150 mM NaCl, 5 mM EGTA, 5 mM glucose, 5 mM MgCl$_2$, pH: 6.1) for 60 seconds at room temperature, followed by 4% PFA. For panNa$_v$ staining, we used 1% PFA + 3% sucrose in PBS. For EB1 staining, we treated fixed neurons using 1 mM EGTA in 100% methanol for 5 minutes at -20°C, followed by 4% PFA for 5 minutes at room temperature. We used 0.5% Triton-X in PBS for 10 minutes to permeabilize the cells and 0.2% BSA in PBS (BSA-PBS) for blocking and washing. Following primary and secondary staining, we washed the cells once in 0.1% Triton-X in PBS and 3 times in BSA-PBS. Primary and secondary antibodies were incubated in BSA-PBS at room temperature for 75 minutes and 45 minutes, respectively. For SIM experiments, we incubated γ/9d overnight at 4°C. We mounted coverslips on glass slides using Immu-Mount (Thermo/Shandon). For SIM experiments, we mounted coverslips on glass slides using ProLong Gold (ThermoFisher). Phalloidin was incubated in PBS for 2 hours at room temperature. For STORM experiments, phalloidin staining was performed immediately before imaging.

For AIS intensity experiments using Tp9, Tp16 and C57Bl6 mouse lines, hippocampal neurons were prepared as previously described (Fath et al., 2009). In brief, hippocampi were dissected from the brains of embryonic mice at embryonic day 16 (E16) and dissociated by mechanical trituration after enzymatic exposure to trypsin and DNase I (Sigma-Aldrich). Cells were plated at a density of 58,000 cells/cm^2 on PDL-coated 12 mm coverslips and maintained in neurobasal media supplemented with 2% B27 and 2 mM Glutamax (Life Technologies) at 37°C and 5% CO_2. Tp9 cultures were transduced at 0 DIV with either CMV-EGFP-Cre or CMV-EGFP adeno-associated viruses (UNC Vector Core Facility) at a concentration of 5 x 10^7 viral particles/70,000 cells. Prior to immunostaining, cultures were fixed at 9 DIV with 4% PFA in PBS for 15 min at room temperature. We then permeabilized the cells using 0.1% TritonX-100 in PBS for 5 min and blocked in 2% FBS in PBS. For Tm4 staining, cells were instead permeabilized for 5 min with ice-cold MeOH and blocked in 2% FBS in PBS. Coverslips were mounted on glass slides using ProLong Gold (Life Technologies).

Plasmids, antibodies and reagents

mCherry-C1 (mCherry) was purchased from Clontech. PAGFP-actin (Dopie et al., 2012) was a kind gift from Maria Vartiainen (University of Helsinki, Finland). YFP-Tpm3.1 and YFP-Tpm3.2 were described previously (Tojkander et al., 2011). shRNA against rat Tpm3.1 (NM_173111.1) was purchased from GeneCopoeia (RSH053175-33-mH1, target sequence CCAAGTCTTAGCCAAACAACA). Mouse monoclonal anti-ankyrin G antibody (1:1000, UC Davis/NIH NeuroMab Facility, Clone 106/36) and mouse monoclonal panNF-186 (1:500, UC Davis/NIH NeuroMab Facility, Clone A12/18) were purchased from NeuroMab. Sheep polyclonal anti-γ/9d (1:100, for SIM: 1:50, AB5447), mouse monoclonal anti-Tpm3 (clone 2G10.2, MAB2256), rabbit polyclonal anti-GluA1 (1:300, Chemicon/Millipore AB1504), chicken polyclonal anti-MAP2 (1:10000, AB5543), chicken anti-β3 tubulin (1:500, AB9354) and mouse anti-ankyrin G (1:500, MABN466) were purchased from Merck Millipore. Rabbit polyclonal anti-panNa$_v$ was purchased from Alomone Labs (1:200, ASC-003). Rabbit anti-myosin IIB (1:500) was purchased from Australian Biosearch (909901). Rabbit anti-TRIM46 (1:100) was described previously (van Beuningen et al., 2015). Mouse anti-EB1 (1:100, 610535) were purchased from BD Transduction Lab. Rabbit anti-GFP (1:1000, AB290) was purchased from Abcam. Rabbit polyclonal δ9d (1:250, purified serum) was produced by the Gunning lab and previously described

(Schevzov et al., 2011). Alexa 647- and Alexa 488-conjugated phalloidin were purchased from ThermoFisher (1 μM, A22287). Alexa Fluor-conjugated secondary antibodies (1:400) were purchased from ThermoFisher. The anti-tropomyosin drugs TR100 and Anisina (ATM3507) were described previously (Currier et al., 2017; Stehn et al., 2016; Stehn et al., 2013) and were added to culture media from 50-mM stock solutions in DMSO. Latrunculin B (Sigma, L5288) was added to culture media from a 2.5-mM stock solution in DMSO.

Generation of the Tpm3 gene exon 1b conditional knockout mouse

Genomic fragments of the *Tpm3* exon 1b region were assembled into a targeting vector containing a Neo cassette flanked by Frt sites located upstream of exon 1b (Supplementary figure 9). LoxP sites were inserted upstream of the Neo cassette and in the 3' region downstream from exon 1b. A diphtheria toxin A (DTA) cassette was used in the targeting construct for negative selection. ES cells were electroporated with the targeting construct and the selected ES cell clones were microinjected into C57Bl/6 blastocysts to generate chimeras containing the targeted allele. Chimeric mice were subsequently bred against Flp transgenic mice to remove the Neo drug selection cassette via Flp-mediated recombination and obtain germline F1 mutants with the conditional knockout allele. Exon 1b can be excised to create the constitutive full knockout allele by Cre-mediated recombination of the LoxP sites in the conditional knockout allele. The conditional knockout allele prior to Cre-mediated recombination was tested by PCR genotyping (Supplementary figure 9b).

Imaging

For taking confocal stacks, we used a Zeiss LSM880 inverted confocal microscope (Zeiss) equipped with a 63x 1.40 NA oil-immersion objective or a Zeiss LSM710 upright confocal microscope (Zeiss) equipped with a 63x 1.46 NA oil-immersion objective. Both microscopes were equipped with 405, 488, 561, and 633 nm laser lines. We adjusted laser power and gain settings as to maximize signal-to-noise ratio while ensuring no pixels were saturated outside the somata. *Z* stacks were acquired at a step size of 0.2 μm. Imaging of fixed samples was performed at room temperature. For live-cell imaging we used a temperature-controlled chamber and CO_2 supply. We imaged live cells in culture media at 37°C and 5% CO_2 using a Zeiss LSM710 upright confocal microscope equipped with a 63x 1.0 NA water-dipping objective. For epifluorescence imaging,

we used a Zeiss Axio Imager Z2 upright epifluorescence microscope (Zeiss) equipped with a 40x 1.3 NA oil-immersion objective and a Hamamatsu Orca Flash 4.0 LT camera (Hamamatsu). Alternatively, we used a Zeiss Axio Imager M1 upright epifluorescence microscope (Zeiss) equipped with a 20x 0.8 NA objective and an AxioCam HRm camera (Zeiss). We used Zeiss Zen software for acquisition.

For SIM, we used a DeltaVision OMX SR imaging system (GE Healthcare Life Sciences) equipped with a 60x 1.42 NA PlanApo N oil objective, 488, 560, and 640 nm laser lines, and 3 sCOMS cameras. We used the AcquireSR software for acquisition and SoftWorx software for image reconstruction and alignment.

For STORM, we used an N-STORM system comprising a Nikon Eclipse Ti-E inverted microscope with Nikon IR-based Perfect Focus System (Nikon Instruments). The microscope was equipped with a 100x 1.49 NA Apo TIRF oil-immersion objective, 405 and 647 nm laser lines (100 and 300 mW, respectively), and an iXon+ 897 camera (Andor). We used a Nikon Intensilight metal arc light source (Nikon) to locate neurons. We used NIS-Elements software for acquisition. We placed the neurons in STORM buffer immediately before imaging: pH 7.9 50 mM Tris, 10% glucose, 70 mM freshly prepared MEA (Sigma), 0.75 mg/ml glucose oxidase (Sigma), and 0.04 mg/ml catalase (Sigma). We continuously illuminated the sample using the 647-nm laser at full power for a series of 20,000-30,000 images of 20-40 ms exposure time (128 x 128 pixels). We used an increasing intensity of 405-nm illumination to reactivate fluorophores. For the analysis of the AIS in mouse hippocampal neurons, fixed samples were imaged on an Axioskop 40 microscope (Zeiss) using a 40x oil objective. AIS intensity was measured using ImageJ software and statistically analyzed in GraphPad Prism (v7.02).

Photoactivation

For photoactivation experiments, live neurons were stained using panNF-186 to label the AISs (Hedstrom et al., 2008). 1-2 hours before imaging, neurons were incubated in culture media containing panNF-186 for 10 minutes at 37°C and 5% CO_2, washed 3 times in Neurobasal media, then incubated in culture media containing anti-mouse Alexa Fluor-647 for 10 minutes at 37°C and 5% CO_2. Neurons were then washed and returned to culture media. We acquired a frame every 3 seconds covering an area of 38.4 x 38.4 μm (256 x 256 pixels) with a pixel dwell time of 3.15 μs. After acquiring 3 pre-activation frames, we used 10-15 iterations of a 405-nm laser at full

power (30 mW) to induce photoactivation. To measure the rate of fluorescence decay we limited the photoactivation to a square region of interest 2.25 x 2.25 μm (15 x 15 pixels). Acquisition was resumed immediately after photoactivation for 360 s at 3-s intervals.

For each experiment, the fluorescence intensity within the region of interest in the pre-activation frames was measured, averaged, and the value was subtracted from subsequent measurements. The first post-activation frame was taken as time-point 0 s. The average fluorescence intensity in subsequent frames (F_t) were normalized to the first frame (F_0) to plot fluorescence decay curves. Decay curves were fit to the two-component exponential function $F(x) = F_1 . e^{\frac{-x}{t1}} + F_2 . e^{\frac{-x}{t2}}$ where x is time, F_1 is the component with the smaller time constant (dynamic pool), F_2 is the component with the larger time constant (stable pool), and t_1 and t_2 are the respective time constants (Star et al., 2002). The proportions of the dynamic and stable pools were calculated as $F_d = \frac{F_1}{F_1+F_2}$ and $F_s = \frac{F_2}{F_1+F_2}$, respectively.

Electrophysiology

For electrophysiological recordings, we placed coverslips in a submerged recording chamber and perfused using an extracellular solution containing (in mM): 124 NaCl, 3 KCl, 1.25 NaH_2PO_4, 1 $MgSO_4$, 26 $NaHCO_3$, 15 D-glucose, 2 $CaCl_2$; bubbled using 5% CO_2/95% O_2 at 32°C. We used patch electrodes (3-5 MΩ) to perform whole-cell recordings in individual cells. Whole-cell pipettes used for current-clamp experiments contained the following (in mM): 130 K-gluconate, 8 NaCl, 10 HEPES, 0.4 EGTA, 4 Mg-ATP and 0.3 Na-GTP, with the addition of either Anisina (2.5 μM) or DMSO (0.2%). The osmolarity of all intracellular solutions was adjusted to 285 mOsm and the pH to 7.25. Action potentials were detected and analyzed using the Mini Analysis Program 5.6.6. (Synaptosoft). Firing frequency was calculated from the interval between the second and the third action potential during a 500 ms depolarizing step evoked by 100-200 pA. Data are expressed as frequency. The phase plane plots were constructed with Clampex software using the first derivative of the somatic membrane potential (dV/dt) versus the somatic membrane potential. Action potential threshold was determined from the first inflection point (here, when the phase plane plot reached 10mV/ms (Naundorf et al., 2006)).

Image Analysis

We used the Fiji software platform for image analysis (Schindelin et al., 2012). We plotted the fluorescence intensity profile ~1-5 μm along the AIS where periodicity was visible in a single plane in a SIM reconstruction, avoiding patches and fasciculations. We used a MATLAB script to locally normalize fluorescence intensity in each profile. We used the "autocorr" function in MATLAB to calculate the autocorrelation function for each profile and obtain autocorrelation curves. We used the "findpeaks" function in MATLAB to detect individual peaks in each profile and note their locations to calculate inter-peak distances.

To quantify the effect of Tpm3.1/2 shRNA knockdown on the accumulation of ankyrin G at the AIS, we used NeuronJ (Meijering et al., 2004) to blindly trace the AISs of transfected neurons expressing either scramble or anti-Tpm3.1/2 shRNA, as well as neighboring non-transfected neurons. We used a 3-μm moving average to smooth fluorescence intensity profiles (van Beuningen et al., 2015) and noted the peak intensity of every profile. Relative ankyrin G fluorescence intensity was calculated by comparing the peak intensity recorded in the transfected neuron to the mean peak intensity of the neighboring non-transfected neurons. We then normalized the mean values to the mean relative intensity of neurons expressing scramble shRNA.

Figure 5B: AIS intensity was measured using the line tool in ImageJ (v1.51s). Briefly, a segmented line was traced along the thickest length of the AIS as indicated by the Ankyrin-G fluorescence signal. ImageJ then measured the signal intensity and length of the area associated with the segmented line. Raw data obtained from ImageJ were exported to excel then GraphPad Prism (v7.02) for statistical analyses.

Figure 10: The AIS region was determined using an Ankyrin G antibody (cat. #MABN466, Merck). Using the corresponding Ankyrin G signal, the fluorescence intensity of myosin IIB (cat. #909901, Australian Biosearch) was measured along the initial 20 μM of the AIS. Image J software was used to measure fluorescence intensity.

For calculating the ALI, we measured the fluorescence intensity profile of either anti-ankyrin G or panNa$_v$ in the initial 30 μm of every neurite in a single neuron. After subtracting background fluorescence, we calculated the 3-μm moving average to smooth the profiles (van Beuningen et al., 2015), trimmed the profiles for even averaging, and then normalized all measurements to the peak intensity value. We then noted the normalized peak value for each neurite and used them to

calculate the median peak value. AIS localization index was expressed as $ALI = 1 - median_{peaks}$ such that a value closer to 1 indicates the strongest accumulation in a single neurite, while a value closer to 0 indicates homogenous concentration across all neurites.

For calculating the ADR, we used NeuronJ (Meijering et al., 2004) to trace the axon and dendrites in confocal stacks. We then used a maximum intensity projection to measure background fluorescence, the mean fluorescence intensity along ~100 μm of the axon distal to the AIS, and the mean fluorescence along all dendrites. ADR was calculated as $ADR = \frac{(F_{axon} - F_{background})}{(F_{dendrites} - F_{background})}$ (Lewis et al., 2009).

We used custom scripts written by Leterrier et al. (2015) to convert STORM localization files into a format readable by the ThunderSTORM plugin (Ovesny et al., 2014), which was used for reconstructing images. For evaluating periodicity, we used MATLAB to fit intensity profiles to a single-term Fourier series represented by $y = a_0 + a_i \cos(iwx) + b_i \sin(iwx)$ and obtained the period length and the R-squared value reflecting goodness of fit.

Colocalization analysis between F-actin (Alexa-488) and Tpm3.1/2 (Alexa 647) -positive signals was performed on maximum intensity projections of SIM images. Importantly, SIM imaging resulted in a slight variability in Z-levels for different fluorophores and therefore based on a visual inspection three consecutive Z-layers at best focus for each fluorophore were manually selected to be included in the maximum intensity projection of a Z-stack. To estimate the error that the Z-level shift (or any technical aspect depending on different fluorophores) gives for the colocalization quantification, we performed the same experiment having double Tpm3.1/2 stainings visualized with 488- and 647-dyes. AIS region was selected for the analysis based on ankyrin G staining (Alexa-594). Regions of interest (ROIs) were hand-drawn outlining the AIS regions.

The 'EzColocalization' Fiji/ImageJ plugin was used for colocalization analysis in ROIs of maximum intensity projections according to the protocol described by (Stauffer et al. 2018). Briefly, each fluorophore channel was subject to automatic thresholding to remove background, and the Pearson correlation coefficient (PCC) was calculated to get a value between -1 and 1, reflecting the degree of co-occurrence of signal intensities between both F-actin and Tpm3.1/2. The value 1 indicates perfectly linearly related intensities, the value −1 perfectly inversely linearly

related intensities and the values near 0 intensities that are uncorrelated with one another (Dunn et al., 2011).

Statistical Analyses

Binomial tests were performed using the SPSS software package. All other statistical analyses were performed using the OriginLab software package. Intensity profiles curves for STORM data were created using MATLAB. All other graphs were created using OriginLab. Data were checked for normality (Shapiro-Wilk test) and homogeneity of variance (Levene's test). For parametric data, we used the independent two-sample *t* test, or one-way ANOVA and Tukey's test for post-hoc analysis. For non-parametric data, we used Kruskal-Wallis ANOVA and Mann-Whitney *U* Test. Bonferroni correction for multiple comparisons was used wherever appropriate. We used Kolmogorov-Smirnov test to compare the distributions of inter-peak distances under different conditions. We created box plots in Tukey style (Krzywinski and Altman, 2014) with the addition of solid black circles to represent the mean. Classification of photoactivation data as belonging to actin patches or areas outside the patches was done using hierarchical cluster analysis. We used double-exponential decay fits of 44 normalized fluorescence decay curves recorded from the AIS, each responding to 120 variables corresponding to fluorescence levels at 120 time points between 0 and 357. This number of time points corresponds to the sampling frequency of the recordings. We ran a hierarchical cluster analysis using Ward's method (squared Euclidean distance, data standardization: range 0-1) that assigned 15 curves as belonging to AIS actin patches, and 29 curves as recorded from areas outside the patches. To test the significance of the difference between the resultant clusters, we performed one-way ANOVA for each time point. The between-groups difference was significant at all time points after 0 s ($p < 0.05$). The difference between recordings from dendrites and areas in the AIS outside the actin patches was not significant at any time point (Tukey's test), while recordings from the patches were significantly different from recordings from both dendrites and areas outside the patches (Tukey's test, $p < 0.05$) for all time points after 0 s.

SUPPLEMENTAL REFERENCES

Currier, M.A., Stehn, J.R., Swain, A., Chen, D., Hook, J., Eiffe, E., Heaton, A., Brown, D., Nartker, B.A., Eaves, D.W., et al. (2017). Identification of Cancer-Targeted Tropomyosin Inhibitors and Their Synergy with Microtubule Drugs. Mol Cancer Ther 16, 1555-1565.

Dopie, J., Skarp, K.P., Rajakyla, E.K., Tanhuanpaa, K., and Vartiainen, M.K. (2012). Active maintenance of nuclear actin by importin 9 supports transcription. Proc Natl Acad Sci U S A 109, E544-552.

Dunn, K.W., Kamocka, M.M., and McDonald, J.H. (2011). A practical guide to evaluating colocalization in biological microscopy. Am J Physiol Cell Physiol 300, C723-742.

Fath, T., Ke, Y.D., Gunning, P., Gotz, J., and Ittner, L.M. (2009). Primary support cultures of hippocampal and substantia nigra neurons. Nat Protoc 4, 78-85.

Hotulainen, P., Llano, O., Smirnov, S., Tanhuanpaa, K., Faix, J., Rivera, C., and Lappalainen, P. (2009). Defining mechanisms of actin polymerization and depolymerization during dendritic spine morphogenesis. J Cell Biol 185, 323-339.

Krzywinski, M., and Altman, N. (2014). Points of Significance: Visualizing samples with box plots. Nat Meth 11, 119-120.

Leterrier, C., Potier, J., Caillol, G., Debarnot, C., Rueda Boroni, F., and Dargent, B. (2015). Nanoscale Architecture of the Axon Initial Segment Reveals an Organized and Robust Scaffold. Cell Rep 13, 2781-2793.

Lewis, T.L., Jr., Mao, T., Svoboda, K., and Arnold, D.B. (2009). Myosin-dependent targeting of transmembrane proteins to neuronal dendrites. Nat Neurosci 12, 568-576.

Meijering, E., Jacob, M., Sarria, J.C., Steiner, P., Hirling, H., and Unser, M. (2004). Design and validation of a tool for neurite tracing and analysis in fluorescence microscopy images. Cytometry A 58, 167-176.

Ovesny, M., Krizek, P., Borkovec, J., Svindrych, Z., and Hagen, G.M. (2014). ThunderSTORM: a comprehensive ImageJ plug-in for PALM and STORM data analysis and super-resolution imaging. Bioinformatics 30, 2389-2390.

Schevzov, G., Whittaker, S.P., Fath, T., Lin, J.J., and Gunning, P.W. (2011). Tropomyosin isoforms and reagents. Bioarchitecture 1, 135-164.

Stauffer, W., Sheng, H., and Lim, H.N. (2018). EzColocalization: An ImageJ plugin for visualizing and measuring colocalization in cells and organisms. Sci Rep 8, 15764.

Stehn, J., Mariana, A., Failes, T., Ashokakumar, V., Eiffe, E., Heaton, A., Hook, J., Sivanandhan, D., Arndt, G., Gunning, P., et al. (2016). Synergistic action of first-in-class anti-tropomyosin compound, ATM-3507 (Anisina) and microtubule targeting inhibitors in pre-clinical models of non-small cell lung cancer (NSCLC). European Journal of Cancer 69, S116.

Stehn, J.R., Haass, N.K., Bonello, T., Desouza, M., Kottyan, G., Treutlein, H., Zeng, J., Nascimento, P.R., Sequeira, V.B., Butler, T.L., et al. (2013). A novel class of anticancer compounds targets the actin cytoskeleton in tumor cells. Cancer Res 73, 5169-5182.

Tojkander, S., Gateva, G., Schevzov, G., Hotulainen, P., Naumanen, P., Martin, C., Gunning, P.W., and Lappalainen, P. (2011). A molecular pathway for myosin II recruitment to stress fibers. Curr Biol 21, 539-550.

van Beuningen, S.F., Will, L., Harterink, M., Chazeau, A., van Battum, E.Y., Frias, C.P., Franker, M.A., Katrukha, E.A., Stucchi, R., Vocking, K., et al. (2015). TRIM46 Controls Neuronal Polarity and Axon Specification by Driving the Formation of Parallel Microtubule Arrays. Neuron 88, 1208-1226.